

# A faint optical flash in dust-obscured GRB 080603A – implications for GRB prompt emission mechanisms

C. Guidorzi<sup>1,2\*</sup>, S. Kobayashi<sup>2</sup>, D. A. Perley<sup>3</sup>, G. Vianello<sup>4</sup>, J. S. Bloom<sup>3</sup>, P. Chandra<sup>5</sup>, D. A. Kann<sup>6</sup>, W. Li<sup>3</sup>, C. G. Mundell<sup>2</sup>, A. Pozanenko<sup>7</sup>, J. X. Prochaska<sup>8</sup>, K. Antoniuk<sup>9</sup>, D. Bersier<sup>2</sup>, A. V. Filippenko<sup>3</sup>, D. A. Frail<sup>10</sup>, A. Gomboc<sup>11,12</sup>, E. Klunko<sup>13</sup>, A. Melandri<sup>14</sup>, S. Mereghetti<sup>4</sup>, A. N. Morgan<sup>3</sup>, P. T. O’Brien<sup>15</sup>, V. Rumyantsev<sup>9</sup>, R. J. Smith<sup>2</sup>, I. A. Steele<sup>2</sup>, N. R. Tanvir<sup>15</sup>, A. Volnova<sup>16</sup>

<sup>1</sup>Physics Department, University of Ferrara, via Saragat 1, I-44122, Ferrara, Italy

<sup>2</sup>Astrophysics Research Institute, Liverpool John Moores University, Twelve Quays House, Egerton Wharf, CH41 1LD, Birkenhead, UK

<sup>3</sup>Department of Astronomy, University of California, Berkeley, CA 94720-3411, USA

<sup>4</sup>INAF - Istituto di Astrofisica Spaziale e Fisica Cosmica Milano, via Bassini 15, I-20133 Milano, Italy

<sup>5</sup>Department of Physics, Royal Military College of Canada, Kingston, ON, Canada

<sup>6</sup>Thüringer Landessternwarte Tautenburg, Sternwarte 5, D-07778 Tautenburg, Germany

<sup>7</sup>Space Research Institute (IKI), 84/32 Profsoyuznaya Str, Moscow 117997, Russia

<sup>8</sup>Department of Astronomy and Astrophysics, UCO/Lick Observatory, University of California, 1156 High Street, Santa Cruz, CA 95064, USA

<sup>9</sup>SRI Crimean Astrophysical Observatory (CrAO), Nauchny, Crimea 98409, Ukraine

<sup>10</sup>National Radio Astronomy Observatory, 1003 Lopezville Road, Socorro, NM 87801, USA

<sup>11</sup>Faculty of Mathematics and Physics, University of Ljubljana, Jadranska 19, SI-1000 Ljubljana, Slovenia

<sup>12</sup>Centre of Excellence SPACE-SI, Aškerčeva cesta 12, SI-1000 Ljubljana, Slovenia

<sup>13</sup>Institute of Solar-Terrestrial Physics, Lermontov st., 126a, Irkutsk 664033, Russia

<sup>14</sup>INAF – Osservatorio Astronomico di Brera, via E. Bianchi 46, I-23807 Merate (LC), Italy

<sup>15</sup>Department of Physics and Astronomy, University of Leicester, University Road, Leicester LE1 7RH, UK

<sup>16</sup>Sternberg Astronomical Institute, Moscow State University, Universitetsky pr., 13, Moscow 119992, Russia

5 November 2018

## ABSTRACT

We report the detection of a faint optical flash by the 2-m Faulkes Telescope North simultaneously with the second of two prompt  $\gamma$ -ray pulses in INTEGRAL gamma-ray burst (GRB) 080603A, beginning at  $t_{\text{rest}} = 37$  s after the onset of the GRB. This optical flash appears to be distinct from the subsequent emerging afterglow emission, for which we present comprehensive broadband radio to X-ray light curves to 13 days post-burst and rigorously test the standard fireball model. The intrinsic extinction toward GRB 080603A is high ( $A_{V,z} = 0.8$  mag), and the well-sampled X-ray-to-near-infrared spectral energy distribution is interesting in requiring an LMC2 extinction profile, in contrast to the majority of GRBs. Comparison of the  $\gamma$ -ray and extinction-corrected optical flux densities of the flash rules out an inverse-Compton origin for the prompt  $\gamma$ -rays; instead, we suggest that the optical flash could originate from the inhomogeneity of the relativistic flow. In this scenario, a large velocity irregularity in the flow produces the prompt  $\gamma$ -rays, followed by a milder internal shock at a larger radius that would cause the optical flash. Flat  $\gamma$ -ray spectra, roughly  $F \propto \nu^{-0.1}$ , are observed in many GRBs. If the flat spectrum extends down to the optical band in GRB 080603A, the optical flare could be explained as the low-energy tail of the  $\gamma$ -ray emission. If this is indeed the case, it provides an important clue to understanding the nature of the emission process in the prompt phase of GRBs and highlights the importance of deep ( $R > 20$  mag), rapid follow-up observations capable of detecting faint, prompt optical emission.

**Key words:** gamma-rays: bursts — radiation mechanisms: nonthermal

## 1 INTRODUCTION

The exact mechanism that produces the prompt radiation of a gamma-ray burst (GRB) is still unknown. As a nonthermal process, synchrotron and inverse Compton (IC) are the main candidates. The former can successfully account for most of the afterglow emission evolution, and is naturally expected from shock-accelerated electrons. As such, this has also been considered for explaining the  $\gamma$ -ray prompt emission itself. However, the energy spectrum of a GRB, usually modelled with a Band function (Band et al. 1993), is such that the typical value for the low-energy photon index ( $\alpha$ ) violates the so-called “synchrotron death line” ( $\alpha = -2/3$ ) for a sizable fraction of cases (Preece et al. 1998; Guiriec et al. 2010; Guidorzi et al. 2011). In addition, the value generally observed,  $\alpha \approx -1$ , differs from the value of  $-3/2$  expected for rapidly cooling electrons (the so-called “fast-cooling death line”; Ghisellini et al. 2000). Although under some assumptions most GRB spectra could be reconciled with a synchrotron origin (e.g., Lloyd & Petrosian 2000; Daigne et al. 2011), the question of whether it is the dominant process in the GRB production remains unanswered.

On the other hand, IC has been considered as a possible alternative, such as synchrotron self-Compton (SSC; Kumar & McMahon 2008), especially when the prompt optical emission is very bright (Racusin et al. 2008). IC as the source of  $\gamma$ -rays requires a soft component in the infrared (IR) through ultraviolet (UV) range for providing the seed photons; this in turn means that the second IC component peaks in the GeV–TeV range, potentially implying an “energy crisis” problem (Piran et al. 2009). Combining prompt optical and  $\gamma$ -ray measurements, together with the wealth of information derived from the broadband modelling of the early-to-late time afterglow, offers a direct way test for IC as the mechanism for the GRB production.

The standard afterglow model (see, e.g., Mészáros 2006 for a review) is rather successful in modelling the temporal and spectral evolution of GRB afterglows. However, models often require modifications, such as energy injections from long-lived internal engines or density enhancements in the surrounding medium, and for a sizable fraction of cases, even these options cannot provide a fully satisfactory explanation (e.g., Melandri et al. 2008).

Long-duration GRBs are also probes of the interstellar and intergalactic medium, and of cosmic star formation history up to redshift  $z \approx 8$  (Salvaterra et al. 2009; Tanvir et al. 2009), potentially exploring the reionization epoch (Kistler et al. 2009; Robertson et al. 2010). Spectral energy distribution (SED) studies and spectroscopic observations can help to shed light, for instance, on the redshift evolution of dust, gas content, and metallicity of the host galaxies of GRBs as well as of the local region within the host (e.g., Prochaska et al. 2007). In addition, they help to identify the crucial physical parameters which favour the production of GRBs. Dust-extinction modelling for a sample of GRB afterglows with well-sampled SEDs has shown that most cases can be described with Small Magellanic Cloud (SMC) profiles (Kann et al. 2010) having little evidence for the 2175 Å bump seen in the Milky Way extinction curve, except for very few cases (Krühler et al. 2008; Prochaska et al. 2009; Elíasdóttir et al. 2009; Perley et al. 2011).

No direct link has been found between the properties of

the prompt emission and those of the circumburst environment surrounding the GRBs and of the host galaxy, such as metallicity (Levesque et al. 2010). Nevertheless, a detailed picture of the properties that can be derived from the broadband afterglow modelling — the dust content and features along the sightline to the GRB within the host galaxy — are crucial to provide a self-consistent description of the entire GRB phenomenon, and for unveiling the yet unknown connections between the GRB itself and its birthplace and (to some extent) progenitor.

This paper reports comprehensive analysis and discussion of the multi-wavelength dataset collected on the long-duration GRB 080603A detected by INTEGRAL (Winkler et al. 2003) in light of the current standard fireball model. This GRB provides an ideal test bed because it had an optical flash simultaneous with the prompt emission, and we recorded the broadband afterglow SED and its evolution. Our dataset includes INTEGRAL data of the  $\gamma$ -ray prompt emission itself, as well as multi-filter photometric and spectroscopic data of the near-infrared/optical afterglow and of the host galaxy. In addition, we analysed the X-ray afterglow data, discovered in the 0.3–10 keV band with *Swift*/XRT (Sbarufatti et al. 2008b), from 3 hours to 7 days after the burst. We also include data from the Very Large Array (VLA), taken from 2 to 13 days post burst, in which the radio afterglow was detected.

Throughout the paper, times are UT and are given relative to the GRB onset time as observed with INTEGRAL, which corresponds to June 3, 2008, 11:18:11 UT. The convention  $F(\nu, t) \propto \nu^{-\beta} t^{-\alpha}$  is followed, where the energy index  $\beta$  is related to the photon index by  $\Gamma = \beta + 1$ . We adopted the standard cosmological model:  $H_0 = 71 \text{ km s}^{-1} \text{ Mpc}^{-1}$ ,  $\Omega_\Lambda = 0.73$ ,  $\Omega_M = 0.27$  (Spergel et al. 2003).

All of the quoted errors are given at 90% confidence level for one interesting parameter ( $\Delta\chi^2 = 2.706$ ), unless stated otherwise.

## 2 OBSERVATIONS

GRB 080603A was detected with the INTEGRAL/IBIS instrument and localised in real time by the INTEGRAL Burst Alert System (IBAS; Mereghetti et al. 2003) with an accuracy of  $3.2'$ . The  $\gamma$ -ray prompt emission in the 20–200 keV energy band lasted about 150 s. A quick-look analysis gave a peak flux of  $0.5 \text{ ph cm}^{-2} \text{ s}^{-1}$ , a fluence of about  $10^{-6} \text{ erg cm}^{-2}$ , and burst coordinates  $\alpha(\text{J2000}) = 18^{\text{h}}37^{\text{m}}38^{\text{s}}.2$ ,  $\delta(\text{J2000}) = +62^{\circ}44'06''$  with an error radius of  $2'$  (Paizis et al. 2008).

The Faulkes Telescope North (FTN) promptly reacted to the IBAS alert and began observing at 11:19:51, which was 100 s after the burst onset time and while prompt  $\gamma$ -ray emission was still ongoing. The automatic GRB pipeline did not identify any candidate; consequently, a pre-programmed *BVRi'* observation sequence with increasingly longer exposure durations was carried out (Guidorzi et al. 2006). However, visual inspection of the frames revealed the presence of an uncatalogued, variable object at  $\alpha(\text{J2000}) = 18^{\text{h}}37^{\text{m}}38^{\text{s}}.1$ ,  $\delta(\text{J2000}) = +62^{\circ}44'39''.4$  with  $R = 19.6 \text{ mag}$  at  $t = 7.37 \text{ min}$ , calibrated against nearby USNOB–1.0 stars (Gomboc et al. 2008). FTN observations continued for 3 hours.

The GRB alert system of the Katzman Automatic Imaging Telescope (KAIT; Li et al. 2003) at Lick Observatory also promptly reacted to the INTEGRAL alert and independently detected the optical counterpart at a position consistent with that of the FTN, reporting  $I = 18.7$  mag at 10.7 min in unfiltered and  $I$ -band images (Chornock et al. 2008). Other robotic telescopes also reported the discovery of the afterglow (Milne & Updike 2008).

We began spectroscopic observations of the optical afterglow with the GMOS dual spectrometer at the Gemini-North 8-m telescope starting at time 13:24, identifying several absorption features at a common redshift of  $z = 1.68742$ , in agreement with preliminary reports (Perley et al. 2008a).

We kept monitoring the evolution of the optical afterglow with the 1.34 m Schmidt telescope of the Thüringer Landessternwarte (TLS), the Liverpool Telescope (LT), the Keck-I 10-m telescope, the Zeiss-1000 and AZT-11 telescopes at the Crimean Astrophysical Observatory (CrAO), and the AZT-33IK telescope at Sayan Observatory up to 4 days post burst (Kann et al. 2008; Rumyantsev & Pozanenko 2008a,b; Perley et al. 2008b; Klunko & Pozanenko 2008; Rumyantsev et al. 2008). From 19 to 22 hours post burst we observed the afterglow at near-infrared (NIR) wavelengths with the Peters Automated Infrared Imaging Telescope (PAIRITEL) through  $JHK$  filters (Miller et al. 2008). Our last detection of the optical afterglow was obtained with the Low Resolution Imaging Spectrometer (LRIS; Oke et al. 1995) 4 days post burst. Two months after the burst we observed the same field with Keck/LRIS using  $u'g'RI$  filters and detected the host galaxy; these observations were subsequently used to subtract the host contribution when the afterglow became comparably faint.

*Swift*/XRT began observing GRB 080603A from 2.9 to 5.9 hours and reobserved it from 2.5 to 7.0 days after the burst. The X-ray afterglow was clearly identified at position  $\alpha(\text{J2000}) = 18^{\text{h}}37^{\text{m}}38^{\text{s}}.06$ ,  $\delta(\text{J2000}) = +62^{\circ}44'40''.1$  with an error radius of  $1''.9$  (Sbarufatti et al. 2008a). During the same time interval *Swift*/UVOT detected the fading afterglow in the  $V$  band (Kuin & Mangano 2008; Sbarufatti et al. 2008b).

Finally, we discovered the radio counterpart with the VLA at 4.86 and 8.46 GHz, initially at the latter frequency with a possible detection at 1.9 days at a flux density of  $116 \pm 41 \mu\text{Jy}$  (Chandra & Frail 2008a). The detection was confirmed at 3.95 days (Chandra & Frail 2008b). Observations continued as late as 13 days post burst.

The Galactic reddening along the direction to the GRB is  $E_{B-V} = 0.044$  mag (Schlegel et al. 1998). The Galactic extinction in each filter has been estimated through the NASA/IPAC Extragalactic Database extinction calculator<sup>1</sup>. Specifically, the extinction in each filter is derived through the parametrisation by Cardelli et al. (1989):  $A_{u'} = 0.23$ ,  $A_B = 0.19$ ,  $A_{g'} = 0.18$ ,  $A_V = 0.14$ ,  $A_{r'} = A_R = 0.12$ ,  $A_{i'} = 0.09$ ,  $A_I = 0.08$ ,  $A_J = 0.04$ ,  $A_H = 0.025$ , and  $A_K = 0.02$  mag.

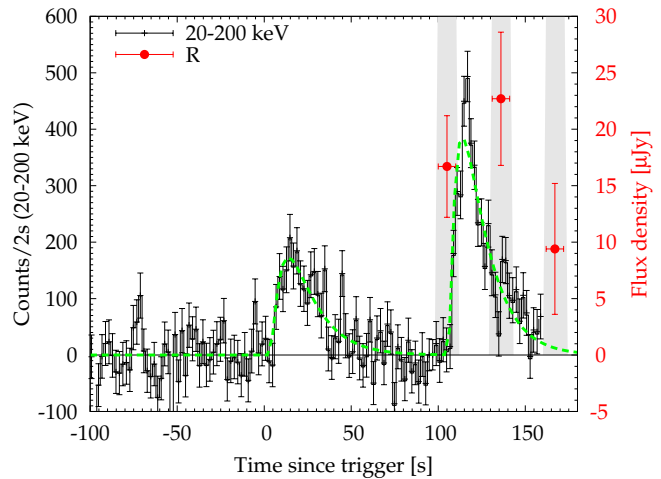


**Figure 1.** INTEGRAL light curve in the 20–200 keV energy band (left-hand ordinate axis). The shaded areas display the time intervals of the first optical measurements with the FTN; the corresponding  $R$ -band flux densities are shown with filled circles (right-hand ordinate axis). The dashed line shows the best-fitting models of the  $\gamma$ -ray pulses as obtained with the model by Norris et al. (2005).

### 3 DATA REDUCTION AND ANALYSIS

#### 3.1 Gamma-ray data

Figure 1 shows the 20–200 keV background-subtracted time profile of GRB 080603A recorded by the IBIS/ISGRI detector (Lebrun et al. 2003). The profile consists of two very similar pulses of duration 30-s, peaking at 14 s and 114 s. A combination of two fast-rise-exponential-decline (FRED)-like pulses as modelled by Norris et al. (2005) gives a satisfactory result ( $\chi^2/\text{dof} = 94.4/81$ ), as shown by the dashed line in Figure 1. The parameters used are the peak time  $t_{\text{peak}}$ , the peak intensity  $A$ , the rise and decay times  $\tau_r$  and  $\tau_d$ , the pulse width  $w$ , and the asymmetry  $k$ . Their best-fitting values are reported in Table 1. Apart from the peak of the second pulse, which is roughly twice as intense as that of the first, the two pulses share very similar temporal properties: rise and decay times around 7 and 20 s, respectively, with a corresponding decay-to-rise ratio around a factor of 3, very typical of classical FREDs (Norris et al. 1996).

Two time-integrated spectra, one for each pulse, show no evidence for spectral evolution: a simple power law can fit both spectra with a  $\gamma$ -ray photon index  $\Gamma_\gamma \approx 1.6$ . Table 2 reports the best-fitting spectral parameters. The 20–200 keV total fluence is  $(1.1 \pm 0.2) \times 10^{-6}$  erg  $\text{cm}^{-2}$ , in agreement with preliminary reports (Paizis et al. 2008). The value of  $\Gamma_\gamma = 1.6$  lying between the typical low-energy and high-energy photon indices of GRB prompt emission spectra (e.g., Kaneko et al. 2006; Sakamoto et al. 2009) suggests that the peak energy,  $E_p$ , is likely to lie within the 20–200 keV energy band. In the context of the sample of GRBs detected with ISGRI and BAT (Vianello et al. 2009), the fluence of GRB 080603A makes it a typical burst.

The corresponding flux-density curve shown in Figure 4 was found to refer to 84 keV; this is the energy at which the energy spectrum with  $\beta_\gamma = \Gamma_\gamma - 1 = 0.6$  has the same value as that averaged over the 20–200 keV range.

Despite the unknown value of  $E_p$ , we can provide a con-

<sup>1</sup> <http://nedwww.ipac.caltech.edu/forms/calculator.html>.

**Table 1.** Best-fitting parameters of the time profile of the  $\gamma$ -ray pulses as seen in the 20–200 keV band.

Pulse	$t_{\text{peak}}$ (s)	$A(\text{at } 84 \text{ keV})$ ( $\mu\text{Jy}$ )	$\tau_r$ (s)	$\tau_d$ (s)	$w$ (s)	$k$
1	$13.7 \pm 1.9$	$18 \pm 2$	$8.0 \pm 2.0$	$21.8 \pm 3.5$	$29.8 \pm 3.8$	$0.46 \pm 0.12$
2	$113.8 \pm 0.9$	$41 \pm 2$	$6.2 \pm 1.1$	$19.4 \pm 1.6$	$25.7 \pm 1.8$	$0.51 \pm 0.08$

**Table 2.** Best-fitting parameters of the energy spectra of the  $\gamma$ -ray prompt emission in the 20–200 keV band. The model is a power-law and  $\Gamma_\gamma$  is the photon index.

Pulse	Time interval (s)	$\Gamma_\gamma$	Average flux ( $10^{-8} \text{ erg cm}^{-2} \text{ s}^{-1}$ )	$\chi^2/\text{dof}$	Fluence ( $10^{-7} \text{ erg cm}^{-2}$ )
1	3–38	$1.6 \pm 0.2$	$1.4^{+0.14}_{-0.6}$	60/64	$4.1 \pm 1.3$
2	100–140	$1.65^{+0.18}_{-0.16}$	$1.9^{+0.16}_{-0.6}$	39/30	$6.7 \pm 1.5$

servative estimate of the isotropic-equivalent radiated energy  $E_{\text{iso}}$  in the GRB rest-frame 1–10<sup>4</sup> keV energy band: we assume that  $E_p$  lies either within or close to the 20–200 keV energy range. In the former case, we use the logarithmic average,  $E_p = 60$  keV, while in the latter case we consider the values 10 keV and 400 keV as the lower and upper boundary, respectively. These values correspond to a 0.3 logarithmic shift from the corresponding boundary, the logarithmic bandwidth being 1. In calculating the fluence in the rest-frame 1–10<sup>4</sup> keV band, the K-correction factor is  $2.8 \pm 0.8$ , where the uncertainty accounts for the different  $E_p$  assumed and where we adopted the typical Band function with  $\alpha_B = -1$  and  $\beta_B = -2.3$  (Kaneko et al. 2006). As a result, we estimate  $E_{\text{iso}} = (2.2 \pm 0.8) \times 10^{52}$  erg and the intrinsic peak energy  $E_{p,i} = 160^{+920}_{-130}$  keV; these values are broadly consistent with the  $E_{p,i}$ – $E_{\text{iso}}$  relation (Amati et al. 2002; Amati 2010), although the poor accuracy on  $E_{p,i}$  is not very constraining.

### 3.2 X-ray data

The *Swift*/XRT began observing GRB 080603A on 2008 June 03 at 14:11:19, about 10.4 ks after the burst, and ended on 2008 June 10 at 11:44:56, with a total net exposure of 17.8 ks in photon counting (PC) mode spread over 6.9 days. The XRT data were processed using the FTOOLS software package (v. 6.7) distributed within HEASOFT. We ran the task XRTPIPELINE (v.0.12.1), applying calibration and standard filtering and screening criteria. Data were acquired only in PC mode due to the faintness of the source. Events with grades 0–12 were selected. The XRT analysis was performed in the 0.3–10 keV energy band.

Source photons were extracted from a circular region centred on the final XRT position (Sbarufatti et al. 2008b) and with a radius of 20 pixels (1 pixel = 2'36), and were point-spread function (PSF) renormalised. Background photons were extracted from nearby circular regions with a total area of  $22.7 \times 10^3$  pixels away from any source present in the field. No pile-up correction was required because of the low count rate ( $\lesssim 0.1 \text{ count s}^{-1}$ ) of the source from the beginning of the XRT observations. When the count rate dropped below  $\sim 10^{-2} \text{ count s}^{-1}$ , we made use of XIMAGE with the tool SOSTA, which corrects for vignetting, exposure varia-

tions, and PSF losses within an optimised box, using the same background region.

We extracted the 0.3–10 keV energy spectrum in the time interval from 10.4 to 21.1 ks; later observations did not allow us to collect enough photons to ensure the extraction of another meaningful spectrum. Source and background spectra were extracted from the same regions as those used for the light curve. Spectral channels were grouped so as to have at least 20 counts per bin. The ancillary response files were generated using the task XRTMKARF. Spectral fitting was performed with XSPEC (v. 12.5). The spectrum can be modelled with an absorbed power law with the combination of XSPEC models WABS ZWABS POW, based on the photoelectric cross section by Morrison & McCammon (1983). Results of the best-fit parameters are reported in Table 6. The Galactic neutral hydrogen column density along the GRB direction was fixed to the value determined from 21 cm line radio surveys:  $N_{\text{HI}}^{\text{Gal}} = 4.7 \times 10^{20} \text{ cm}^{-2}$  (Kalberla et al. 2005). The additional X-ray absorption, modelled in the GRB rest frame, was found to be  $N_{\text{HI},z} = 6.6^{+6.2}_{-4.6} \times 10^{21} \text{ cm}^{-2}$ , very typical of X-ray afterglow spectra (e.g., Campana et al. 2010). The X-ray photon index in the 0.3–10 keV energy band is  $\Gamma_X = 2.3 \pm 0.3$ .

The X-ray unabsorbed flux light curve was derived from the rate curve by assuming the same counts-to-energy factor ( $5.4 \times 10^{-11} \text{ erg cm}^{-2} \text{ s}^{-1} \text{ count}^{-1}$ ) obtained from the spectrum described above. This implicitly relies on the lack of strong spectral evolution from  $\sim 10$  ks onward; although such an assumption cannot be proven due to the paucity of photons at late times, this is in agreement with what is observed for most GRBs (e.g., Evans et al. 2009). Finally, the flux-density curve shown in Figure 4 was calculated at 2.4 keV, the energy at which the energy spectrum with  $\beta_X = \Gamma_X - 1 = 1.3$  has the same value as that averaged over the 0.3–10 keV range.

### 3.3 Infrared/optical data

The FTN carried out robotically triggered observations between 100 s and 190 min. During the detection mode, consisting of the first  $3 \times 10$  s frames in the *R* band, the optical afterglow was too faint to be automatically identified, so the GRB pipeline LT-TRAP (Guidorzi et al. 2006) triggered the multi-filter (*BVRi*) observation sequence with

increasingly longer exposures. However, a quick visual inspection of the data led to the identification of an uncatalogued and variable source proposed to be the afterglow candidate (Gomboc et al. 2008). Our best estimate for the optical afterglow position is  $\alpha(\text{J2000}) = 18^{\text{h}}37^{\text{m}}38^{\text{s}}.05$ ,  $\delta(\text{J2000}) = +62^{\circ}44'39''.4$  with an error radius of  $0''.5$ , and it lies within the final XRT error circle.

The afterglow observations with the FTN occurred during the onset of the second  $\gamma$ -ray pulse; concurrently, a faint optical flash with an  $R$  magnitude varying within the 20–21 range was observed (Fig. 1). The flash was soon followed by a steep rise and a broad plateau around  $10^3$  s, at the end of which a smooth transition to a typical power-law decay with index around 1 took place (Fig. 4).

Later observations were carried out with the LT from 15.5 to 17.1 hours with the Sloan Digital Sky Survey (SDSS)  $r'$  and  $i'$  filters, as well as with the FTN from 21.4 to 26.4 hours in  $i'$ .

Calibration of the  $BVRr'i'$  frames was performed by comparing with the magnitudes of four nonsaturated field stars. The corresponding zero points were determined through the observations of Landolt (1992) field stars for which Smith et al. (2002) provide an SDSS calibration. In both cases the zero points were stable during the night, showing fluctuations as large as 0.02–0.03 mag in the worst cases. Finally, we corrected for the airmass. Both aperture and PSF photometry was systematically carried out using the Starlink GAIA software<sup>2</sup>, making sure that both gave consistent results within the uncertainties. Magnitudes were converted into flux densities ( $\mu\text{Jy}$ ) following Fukugita et al. (1995, 1996). Results are reported in Table 8; magnitudes are corrected for airmass, while flux densities are also corrected for Galactic reddening.

KAIT observations began at  $t = 253$  s in the  $V$ ,  $I$ , and unfiltered bands; the pre-programmed exposure durations generally increased with time. The earliest firm unfiltered detection of the optical afterglow occurred at  $t \approx 11$  min (Chornock et al. 2008), independent of the FTN detection. Successive stacked frames also gave a later detection with the  $I$  filter, while the  $V$  filter only provided either upper limits or very marginal detections, as reported in Table 8. For the  $V$  filter, we also considered the UVOT photometric points provided by Sbarufatti et al. (2008b). We used some of the four FTN field stars to calibrate the KAIT field; for the unfiltered frames we adopted the zero point of the  $R$  band. The last useful frame obtained with KAIT was acquired at 20 min. Despite the large uncertainties, both the measured values and upper limits are in agreement with the contemporaneous values obtained with the FTN, as shown by Figure 4.

At a midpoint time of 1.55 days we observed GRB 080603A with the 1.34-m Schmidt TLS, obtaining a total of  $6 \times 600$  s images in the  $R$  band (Kann et al. 2008). Stacking all six frames, the afterglow is detected. In order to subtract the contribution from the extended object later identified as the host galaxy and properly account for the crowded field, another frame of the same field was taken on 2008 August 26 and used for image subtraction with the ISIS

package<sup>3</sup> (Alard & Lupton 1998). The brightness, estimated with both aperture photometry and SExtractor (v. 2.5.0; Bertin & Arnouts 1996), is  $R = 22.1 \pm 0.3$  mag.

Other late-time observations with  $R$  filters were obtained with the 1.25-m AZT-11 (at 0.36 days) and 1-m Zeiss-1000 (Z1000, at 1.6 and 3.6 days) telescopes of the Crimean Astrophysical Observatory (CRAO; Rumyantsev & Pozanenko 2008a,b; Rumyantsev et al. 2008), and with the 1.5-m AZT-33IK telescope (at 0.30 days) of the Sayan Observatory (Klunko & Pozanenko 2008). In all cases the afterglow was detected, except for the last observation at 3.6 days, which provided an upper limit of  $R > 22.9$  mag. For the same reasons as in the case of the TLS frame, we had to correct the measured  $R$  magnitude at 1.6 days for the host-galaxy contribution. Given the lack of late-time images, we merely subtracted the host-galaxy flux contribution as estimated with Keck (see below); this turned into a shift of 0.2 mag in  $R$ , comparable with the uncertainty affecting the measurement itself, which in the end was  $R = 22.52 \pm 0.25$  mag.

The 1.3-m PAIRITEL started observing the afterglow of GRB 080603A at 18.9 hours with  $JHK_s$  filters. Photometric calibration was done against seven nearby 2MASS stars; magnitudes were estimated with both aperture and PSF photometry under GAIA. The NIR afterglow counterpart is clearly detected in all filters in two mosaic frames centred at 0.82 and 0.95 days with 2822 s and 4363 s total exposures, respectively. Our estimates agree within uncertainties with the preliminary results (Miller et al. 2008).

### 3.3.1 Late-time host galaxy observations

We used the Keck LRIS to observe GRB 080603A at two different epochs. The first run was taken on 2008 June 7, between times 12:31 and 12:47 with  $R$  (total exposure 690 s) and  $g'$  (total exposure 785 s) filters. The average airmass was 1.38 and the D560 dichroic was used. The afterglow was clearly detected with both filters at the FTN position.

The same field was reobserved on 2008 August 2, with  $R$  (total exposure 930 s) and  $g'$  (total exposure 1110 s) filters. The average airmass was 1.58 and the D560 dichroic was used. The next night, we observed with the  $u'$  and  $I$  filters (total exposure 720 s each), using the D680 dichroic, with an average airmass of 2.00.

Calibration was based on the identification of seven common field stars having  $R = 20$ – $23$  mag, bright enough to be accurately measured in the stacked images of the FTN+LT and faint enough to avoid saturation in the Keck images. Transformations between the SDSS and Johnson-Cousins systems for this set of faint stars were done following Jordi et al. (2006). The scatter in the zero point of each filter was incorporated into the uncertainties.

In order to subtract the contribution of the host galaxy from the afterglow flux observed at 4.1 days, we performed image subtraction with ISIS. Figure 2 shows the result in the  $R$  band: the afterglow plus host at 4.1 days, the host two months later, and the difference between the two are shown in the left, middle, and right panels, respectively. From image subtraction, we estimated  $R = 24.17 \pm 0.14$  and

<sup>2</sup> <http://starlink.jach.hawaii.edu/starlink>.

<sup>3</sup> <http://www2.iap.fr/users/alard/package.html>.

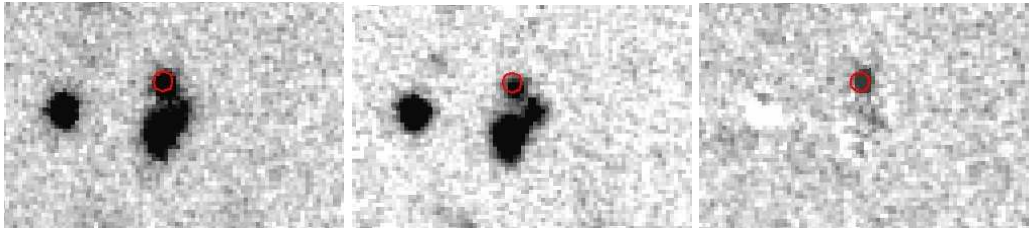


**Figure 2.** Keck-LRIS  $R$ -band images of the crowded field of GRB 080603A. The circle is our best position of the optical afterglow obtained from early FTN frames with  $0''.5$  error radius. *Left panel:* taken at 4.1 days; the afterglow is still detected. *Middle panel:* taken two months after the burst; the host galaxy is clearly visible within the error circle, while the afterglow is no longer detectable. *Right panel:* subtracted image.

**Table 3.** Host-galaxy magnitudes.

Filter	$\lambda_{\text{eff}}$ ( $\text{\AA}$ )	Magnitude	Corrected <sup>a</sup>
$u'$	3450	$25.6 \pm 0.4$	$25.4 \pm 0.4$
$g'$	4731	$24.78 \pm 0.16$	$24.60 \pm 0.16$
$R$	6417	$24.03 \pm 0.12$	$23.91 \pm 0.12$
$I$	7599	$23.98 \pm 0.15^{\text{b}}$	$23.89 \pm 0.15^{\text{b}}$

<sup>a</sup> For Galactic extinction.

<sup>b</sup> Calibration was done against  $i'$  magnitudes of the field stars, corresponding to  $\lambda_{\text{eff}} = 7439 \text{ \AA}$ .

$R_{\text{host}} = 24.03 \pm 0.12$  mag for the afterglow and the host, respectively. Correspondingly, we found  $g' = 24.95 \pm 0.20$  and  $g'_{\text{host}} = 24.78 \pm 0.16$  mag. We also used the late-time  $R$  and  $I$  frames to subtract the host contribution from the observations performed with the FTN and LT at  $t \approx 1$  day, when the afterglow brightness was around 21 mag in the same filter. In the two cases this turned into a shift of  $\sim 0.1$  mag, similar to the corresponding statistical uncertainties. For the same reasons, we did not correct the comparably faint afterglow magnitudes of the optical flash seen in the first FTN images, because of their relatively large uncertainties.

The  $u'$ -band magnitude of the host was calibrated with observations of three standard stars in the PG 0231+051 Landolt (1992) field taken the same night with an airmass of 1.0. Assuming an extinction coefficient in the range 0.36–0.4, the zero point for the  $u'$ -band filter was estimated to be  $Z = 27.8 \pm 0.3$  mag. Table 3 reports the photometry of the host galaxy.

The host centroid, as determined with SExtractor, is  $\alpha(\text{J2000}) = 18^{\text{h}}37^{\text{m}}38^{\text{s}}.03$ ,  $\delta(\text{J2000}) = +62^{\circ}44'39''.0$ , which is  $0''.4$  away from the afterglow position. This angular offset corresponds to a projected distance of 3.4 kpc. Taking into account the uncertainty in the afterglow position, an upper limit of 6 kpc is more conservative, in agreement with the typical projected offsets of long-duration GRBs (Bloom et al. 2002).

### 3.3.2 Spectroscopy

We initiated observations of the GRB afterglow with the Gemini/GMOS dual spectrometer starting at time 13:24 for a series of two 1200 s exposures using the R400 grating, offset by  $\sim 5 \text{ \AA}$  to fill in the detector gaps. The data were

reduced with the LowRedux pipeline<sup>4</sup> developed by J.X.P. and J. Hennawi. This custom software bias subtracts, flat-fields, and optimally extracts the spectra. The two exposures were coadded, weighting by signal-to-noise ratio (S/N); the resultant spectrum has a S/N exceeding 80 per pixel over the range  $\lambda \approx 5000\text{--}8000 \text{ \AA}$ .

The spectrum reveals a series of very strong rest-frame UV transitions at  $z = 1.68742$  that includes Al III  $\lambda\lambda 1854$ , 1862, Zn II  $\lambda 2026$ , Mg II, and a plethora of Fe II resonance and fine-structure transitions (Fig. 3). The detection of the fine-structure transitions uniquely identifies this gas (and redshift) with the host galaxy of GRB 080603A (Prochaska et al. 2006). We have also detected two intervening Mg II systems along the sightline at  $z = 1.2714$  and  $z = 1.5636$ . The former marks yet another example of a strong (equivalent width  $W_{2796} > 2 \text{ \AA}$ ) Mg II system along a GRB sightline (Prochter et al. 2006). Table 9 lists the equivalent-width measurements (from Gaussian fits to the absorption lines) for all of the features detected in our spectrum. Note that the total equivalent width is reported for transitions that are severely blended.

### 3.4 Radio data

GRB 080603A was observed with the VLA<sup>5</sup> at four epochs in the 8.5 GHz band and at 2 epochs in the 4.9 GHz band. Our observations spanned from 2008 June 5 until June 16. That on June 5 was made in the VLA C-configuration, whereas the later observations were made in the DnC-configuration. We adopted the VLA calibrator J1835+613 for phase calibration at both frequency bands.

The data were analysed using standard data-reduction routines of the Astronomical Image Processing System (AIPS). 3C 286 was used for the flux calibration. We had a possible detection ( $\sim 2.8\sigma$ ) in the first observation at 8.5 GHz; it was confirmed in the subsequent observations. The results are reported in Table 4.

<sup>4</sup> <http://www.uchicago.edu/~xavier/LowRedux/index.html>.

<sup>5</sup> The NRAO is a facility of the National Science Foundation (NSF), operated under cooperative agreement by Associated Universities, Inc.

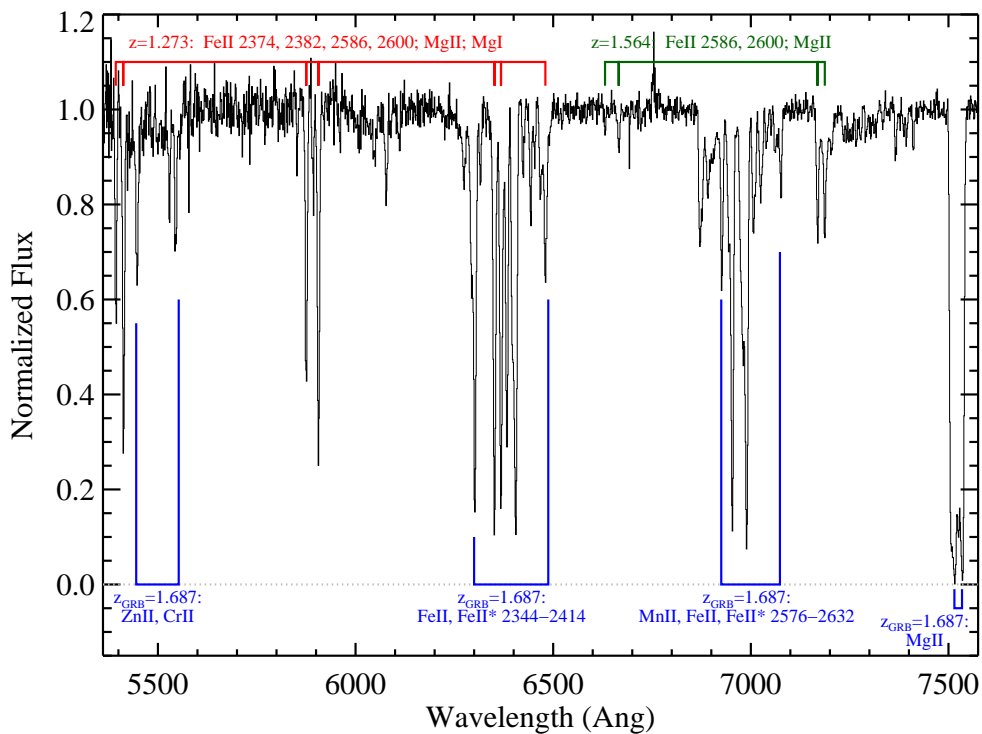


Figure 3. Gemini/GMOS spectrum of the afterglow taken at 2.1 hours post burst.

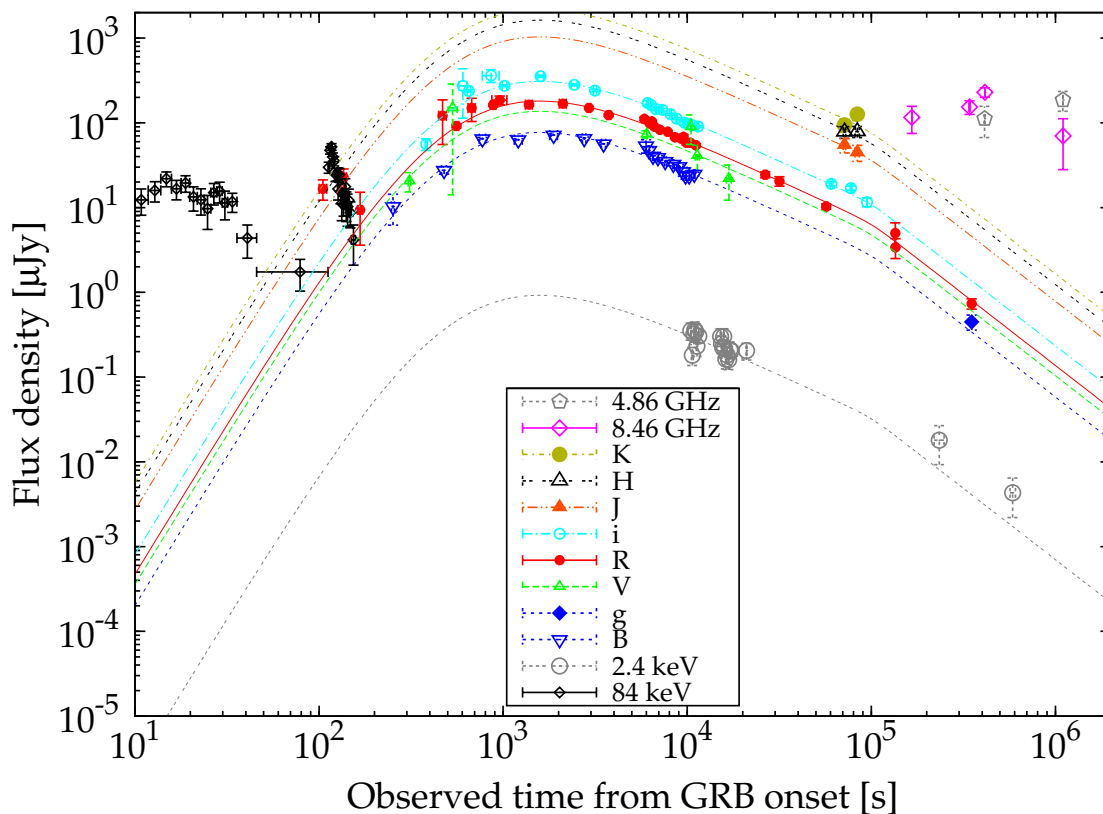


Figure 4. Panchromatic light curves of the prompt and afterglow emissions.



**Table 4.** Flux densities of the radio afterglow obtained with the VLA.

UT Date	$\Delta t$ (days)	$\nu$ (GHz)	$F_\nu$ ( $\mu\text{Jy}$ )
June 05.39	1.92	8.46	$116 \pm 41$
June 07.42	3.95	8.46	$154 \pm 28$
June 08.24	4.77	4.86	$112 \pm 45$
June 08.26	4.79	8.46	$230 \pm 29$
June 16.19	12.72	4.86	$186 \pm 49$
June 16.21	12.74	8.46	$70 \pm 42$

## 4 RESULTS

### 4.1 Multi-band light curves

Figure 4 shows the  $\gamma$ -ray prompt and broadband afterglow light curves. In modelling the data we initially allowed colour change between  $5 \times 10^3$  and  $10^5$  s, i.e. the best-sampled interval, by fitting the data with the sum of a fast-decaying component and a slow-decay component. The colour change between the two was  $0.225 \pm 0.344$ , so less than  $1\text{-}\sigma$ . Depending on whether or not we allow colour change, the results do not change within uncertainties. Given the apparent lack of chromatic changes, to better constrain the evolution we simultaneously fitted the light curves of the various bands (except at the radio wavelengths) with the same function, only allowing different normalisations and no colour change. We modelled the different power-law regimes with the smoothly broken power-law model parametrisation by Beuermann et al. (1999). Furthermore, given the clear presence of a break in the  $R/r'$  and  $B/g'$  curves around  $10^5$  s, we allowed a further achromatic break. The final model is described by Equation (1).

$$F(t) = F_0 \frac{\left[ 1 + \left( \frac{t}{t_{b2}} \right)^{n_2} \right]^{(\alpha_2 - \alpha_3)/n_2}}{\left[ \left( \frac{t}{t_{b1}} \right)^{n \alpha_1} + \left( \frac{t}{t_{b1}} \right)^{n \alpha_2} \right]^{1/n}} \quad (1)$$

The best-fitting solution was found through minimisation of the overall  $\chi^2$ , resulting from the sum of the total  $\chi^2$  values of the individual light curves with respect to each corresponding model. The free parameters are the following:  $\alpha_1$ ,  $\alpha_2$ , and  $\alpha_3$  are the power-law indices during the initial rise, the following decay, and the final ( $> 10^5$  s) decay, respectively. The two break times are  $t_{b1}$  and  $t_{b2}$ , while  $n$  and  $n_2$  are the smoothness parameters regarding the first and second breaks, respectively. Only  $n_2$  could not be determined from the fit because of the sparseness of the data around the final break and it was therefore fixed to 10, so as to give a rather sharp break. The normalisation term is represented with  $F_0$  in Equation (1), although in practice the free parameter we used for each profile was the flux density calculated at a fixed reference time (we chose  $1.5 \times 10^4$  s, close to the time of most observations). The purpose of this choice is to limit the effects of the strong correlations between some parameters, such as  $\alpha_1$  and  $t_{b1}$ , on the determination of the confidence intervals for each parameter.

Concerning the late-time  $g'$  point, we converted its flux density into that corresponding to the close-in-frequency  $B$  band by the factor  $f = (\nu_B/\nu_g)^{-\beta_{\text{obs}}} \approx 0.9$ , where  $\beta_{\text{obs}} = 2$  is the observed spectral index of the SED at the observed

**Table 5.** Multi-filter light curve best-fitting parameters.

Parameter	Value	Unit
$\alpha_1$	$-3.6 \pm 1.7$	
$t_{b1}$	$610_{-251}^{+470}$	s
$\alpha_2$	$0.99 \pm 0.07$	
$n$	$0.30_{-0.13}^{+0.23}$	
$n_K$	$505_{-113}^{+145}$	$\mu\text{Jy}$
$n_H$	$378_{-77}^{+97}$	$\mu\text{Jy}$
$n_J$	$240_{-60}^{+81}$	$\mu\text{Jy}$
$n_i$	$73 \pm 3$	$\mu\text{Jy}$
$n_r$	$42.0 \pm 1.5$	$\mu\text{Jy}$
$n_V$	$32.2_{-5.0}^{+6.0}$	$\mu\text{Jy}$
$n_B$	$18.0 \pm 0.9$	$\mu\text{Jy}$
$n_X$	$0.22 \pm 0.03$	$\mu\text{Jy}$
$t_{b2}$	$1.0_{-0.4}^{+0.6}$	$10^5$ s
$\alpha_3$	$1.7_{-0.3}^{+0.4}$	
$\chi^2/\text{dof}$	$102.4/86$	

visible wavelengths (Section 4.2). This allows us to better constrain the late-time break, in addition to that offered by the  $R$ -band curve. The same correction was applied to the few  $r'$  flux-density points to shift them into the  $R$  band.

This correction introduces a negligible systematic uncertainty. We verified this by alternatively fitting a SED derived by treating all the filters separately, and the best-fitting parameters and corresponding uncertainties turned out to fully agree with the values obtained by merging the filters above mentioned and presented in Section 4.2 (see also Kann et al. 2011).

The best-fitting models are shown in Figure 4 and the corresponding best-fitting parameters are reported in Table 5, where the normalisation terms are expressed as flux densities calculated at  $1.5 \times 10^4$  s.

The peak time,  $t_p$ , is a function of the free parameters as expressed by Equation (2):

$$t_p = t_{b1} \left( \frac{-\alpha_1}{\alpha_2} \right)^{1/n(\alpha_2 - \alpha_1)} = 1575_{-250}^{+430} \text{ s} \quad (2)$$

The uncertainty in  $t_p$  was calculated through error propagation, taking into account the covariance of parameters. Equation (2) is exact only when no further breaks are present — that is, when  $t_{b2} = \infty$  (or, equivalently,  $\alpha_3 = \alpha_2$ ). In practice, it still holds provided that  $t_{b2} \gg t_p$ , as in this case.

From the fit we excluded the earliest points at  $t < 155$  s, connected with the optical flash observed contemporaneously with the last  $\gamma$ -ray pulse (see Fig. 4). We accounted for the presence of some degree of variability around the best-sampled curves, particularly around the broad peak at  $t_p$ , by adding in quadrature a systematic error to the statistical ones (7%, 4%, and 8% for the  $B$ ,  $V$ , and  $i'$  curves, respectively), so as to yield a satisfactory goodness of the fit:  $\chi^2/\text{dof} = 102.4/86$  ( $p$ -value of 11%). The reason for the additional errors was to avoid the risk of underestimating the fit parameters' uncertainties. We also note that the nature of this additional systematic scatter cannot be entirely ascribed to unaccounted variability of the zero points; at least a few percent must genuinely characterise the afterglow light curve. Indeed, the largest deviations from the models are seen to occur *simultaneously* and to *correlate* in all of



the more densely sampled curves:  $B$ ,  $R$ , and  $i'$ . Such deviations are mostly observed within the interval 500–1000 s (final part of the rise) and around  $10^4$  s, at the beginning of the decay.

We alternatively adopted a different log-likelihood function, one more general than that connected with the  $\chi^2$  of equation (1) in that it treats the additional systematic errors as free parameters. In practice, this approach does not provide any noticeable difference in the best-fitting parameters and uncertainties, and the physical implications discussed in Section 5 are completely unaffected. The only difference concerns the systematic error affecting the  $B$ -filter values, for which the alternative log-likelihood provides a systematic error compatible with zero within uncertainties. In any case, this does not affect the best-fitting model to any noticeable degree.

Admittedly, because of the paucity of NIR points (only two, very close in time in each filter), the fitting models in Figure 4 at the corresponding wavelengths assume an achromatic evolution extended to the NIR bands. At first glance this may seem too arbitrary, as there have been GRBs, particularly those with SEDs that are temporally well resolved, for which some chromatic evolution was observed, such as GRB 061126 (Perley et al. 2008c), GRB 071025 (Perley et al. 2010), and GRB 080319B (Bloom et al. 2009; Racusin et al. 2008). Nonetheless, we note that no chromatic evolution was required by comparably early-time observations of several other GRBs (e.g., Krühler et al. 2009; Nysewander et al. 2009; Yuan et al. 2010; Covino et al. 2010; Perley et al. 2011).

Such an assumption has also been made implicitly for the X-ray data; these are too sparse to be modelled independently. Our results show that the X-ray light curve can be described with the same rigid model as the NIR/optical, but of course other possibilities cannot be ruled out. Furthermore, the two latest X-ray points in Figure 4 assume the same spectral shape as that observed around  $1.5 \times 10^4$  s due to paucity of X-ray photons observed after  $10^5$  s (Section 3.2). Although the X-ray photon index of 2.3 observed at  $10^4$  s is not expected to significantly evolve, the assumption of no X-ray spectral evolution from  $10^4$  s to  $10^5$  s must be pointed out.

The radio data clearly show a different behaviour: the peak of the afterglow spectrum crosses the radio bands a few days later. Because of this, they were not considered in the achromatic modelling, but deserve a dedicated analysis in the framework of the standard afterglow model discussed in Section 5.1.

## 4.2 Spectral energy distribution

We derived an SED from the multi-filter light-curve fitting. Although this is based on the achromatic evolution and, as such, does not refer to a particular epoch, we considered the reference time  $t_{\text{ref}} = 1.5 \times 10^4$  s as the most representative of it: this is the midpoint time of the X-ray data, when the high-energy end of the SED does not rely on any assumption. Figure 5 displays the resulting GRB rest-frame SED.

We considered two different models, either a simple power-law and a broken power law with a cooling break,  $\Delta\beta = 0.5$ , combined with three different extinction profiles according to the parametrisation of Pei (1992): SMC, LMC2

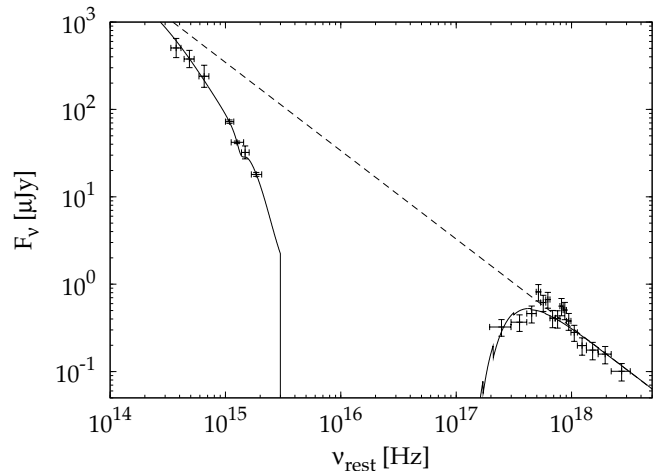


**Figure 5.** Rest-frame SED at  $1.51 \times 10^4$  s. The solid line shows the best-fitting power law with a LMC2 dust-extinction profile. The dashed line shows the same unextinguished power law.

(for the Large Magellanic Cloud), and Milky Way (MW). Note that while Pei’s measurements of the average MW and SMC extinction curves are generally consistent with recent estimates (e.g., Gordon et al. 2003), the LMC implementation is representative only of the area around 30 Doradus (the LMC2 supershell); hence, we denote this curve as LMC2 in this work. The average LMC curve is much more similar to that of the Milky Way.

Table 6 reports all of the results of fitting the SED with different extinction profiles and/or different models at different energy ranges. The uncertainties on the best-fitting parameters include the dependence of the effective frequency of each filter on the folded model. Interestingly, only the LMC2 profile can satisfactorily account for the NIR/optical SED, possibly including the presence of the 2175 Å bump. The dust content is remarkable: the rest-frame extinction is  $A_{V,z} = 0.80 \pm 0.13$  mag, one of the highest among GRBs having observed optical afterglows (Kann et al. 2010). The other two models, MW and SMC, are ruled out. Concerning the models, a simple power law from NIR to X-rays provides a very good result, with  $\beta_{\text{ox}} = 1.01 \pm 0.05$ .

The quality of the photometric set derived for GRB 080603A allows us to attempt a full parametric dust characterisation using the general parametrisation of the Local Group extinction laws by Fitzpatrick & Massa (1990) (hereafter FM), like with GRB 080607 (Perley et al. 2011). In our analysis the parameters  $c_1$ ,  $c_2$ , and  $R_V$  were all tied to each other, as for GRB 080607. The other parameters that were fixed are  $\gamma$  to 1 and  $c_4$  to 0.6, respectively accounting for the 2175 Å bump width and for the strength of the far-UV rise. The free parameters were  $\beta = 0.98 \pm 0.04$ ,  $A_{V,z} = 0.57 \pm 0.19$ ,  $R_V = 2.14 \pm 0.33$ , and  $c_3 = 1.76 \pm 0.66$  (strength of the 2175 Å bump) with  $\chi^2/\text{dof} = 19.8/18$ . Indeed, comparing with the corresponding values for the LMC2 supershell,  $R_V = 2.76 \pm 0.09$  and  $c_3 = 1.46 \pm 0.12$  (Gordon et al. 2003), confirms that the FM model converges to values generally consistent with those of the LMC2 profile. In particular, the  $3\sigma$  nonzero value of  $c_3$  shows that the 2175 Å bump is likely to be present.

As a further check, we folded the spectral models with the filters’ transmission curves and iteratively found the new

effective frequencies at which the model flux densities were the same as the folded ones. We recalculated the best-fit model based on the new effective frequencies. This sequence was repeated until the best-fitting parameters converged to a stable solution. The final effective frequencies changed by 5% at most from the corresponding nominal values which had not been folded with the transmission curves. The best-fitting parameters and the possible evidence for the 2175 Å bump were confirmed with the same confidence.

Although a broken power-law model cannot be ruled out, in this case the break frequency must lie within the soft end of the X-ray band. We therefore conclude that the break frequency (if any) must lie either outside the optical to X-ray range or within the X-ray band itself.

Figure 7 shows a SED at  $4.1 \times 10^5$  s including two radio-flux measurements. Under the assumption that there is no break frequency between radio and visible filters apart from the peak synchrotron frequency  $\nu_m$ , we tried to model the radio points as lying in the  $F_\nu \approx \nu^{1/3}$  power-law segment for  $\nu < \nu_m$  in the slow-cooling regime (Sari et al. 1998) with the cooling frequency lying above the X-rays. We extrapolated the optical flux densities of  $R$  and  $g'$ , the only filters with observations taken at a comparable epoch, assuming the temporal decay of Section 4.1. The X-ray spectrum was also rescaled accordingly. We assumed a negligible contribution from the reverse shock. This would allow us to constrain  $\nu_m$  at the same time: it turns out to be  $\nu_m(1+z) = (4.4 \pm 0.8) \times 10^{12}$  Hz in the GRB rest frame (dashed-dotted line in Fig. 7). However, as will be shown in Section 5.1.1, this clashes with the observed temporal evolution of the afterglow, particularly in the radio band: from the light curve at 8.46 GHz  $\nu_m$  must have crossed the radio band immediately thereafter, around  $4.4 \times 10^5$  s. This would imply an unreasonably fast decay of  $\nu_m$ . In addition, the resulting peak flux of 1.2 mJy is much higher than that observed in the radio when  $\nu_m$  crossed it.

### 4.3 Optical flash

Figure 4 clearly shows that the flux densities at optical and  $\gamma$ -ray wavelengths during the optical flash that occurred simultaneously with the last  $\gamma$ -ray pulse are nearly equal. The corresponding average spectral index is therefore  $\beta_{\text{opt}-\gamma} \approx 0$ . Given the considerable amount of dust, the dust-corrected optical flux increases by a factor of  $\sim 7$ , obtained by the LMC2 extinction profile that best fits the SED at the GRB rest-frame frequency of  $1.3 \times 10^{15}$  Hz, corresponding to the observed  $R$  filter. We point out that the dust considered here is that within the host galaxy, since the Galactic term had already been removed. Replacing the observed optical flux density with the dust-corrected value, the average spectral index becomes  $\beta_{\text{opt}-\gamma} = 0.13$ . The  $\gamma$ -ray spectral index during the last pulse is  $\beta_\gamma = 0.65 \pm 0.2$  (Table 2).

On the one hand, a simple extrapolation of the  $\gamma$ -ray spectrum to optical wavelengths overpredicts the dust-corrected optical flux by  $2 \pm 1$  orders of magnitude; this has already been observed for other bursts with optical detections during the prompt emission (Yost et al. 2007; note that these authors adopted a different convention for the sign of  $\beta$ ). On the other hand, given the intermediate value of  $\beta_\gamma$  lying between the most common values of 0 and 1.3

expected for the low-energy and high-energy indices (respectively) of a typical Band function,  $E_p$  could lie either within or close to the 20–200 keV band with a low-energy index close to 0, as we argued in Section 3.1. In this context, the dust-corrected  $\beta_{\text{opt}-\gamma}$  value is fully consistent with the low-energy index distribution observed in the prompt spectra of most GRBs (Kaneko et al. 2006) and the optical flux density would match the extrapolation of the prompt  $\gamma$ -ray spectrum. However, a broadband flat spectrum and a correspondingly flat electron energy distribution is somewhat nonstandard in the synchrotron shock model.

An interesting possibility proposed in the literature interprets the optical flash as the result of internal shocks with lower velocity irregularities at larger radii, as suggested for the flash of GRB 990123 (Mészáros & Rees 1999).

Temporal analysis of both profiles adds little information: because of the relatively coarse optical sampling of FTN, a correlation between the optical and  $\gamma$ -ray fluxes is neither confirmed nor ruled out. This was tested by integrating the  $\gamma$ -ray counts in the time windows of the optical frames and by comparing the relative variations between the two bands. Although the three optical points exhibit the same behaviour as the  $\gamma$ -rays, both cases (correlation or lack thereof) are compatible with the data within uncertainties.

Although the measured optical flux can be the low-energy extrapolation of the prompt  $\gamma$ -ray emission, in Section 5.2 we test the possibility that the  $\gamma$ -rays are upscattered photons of the optical flash, as suggested for other GRBs to overcome the problems of the synchrotron model (e.g., Kumar & McMahon 2008, Racusin et al. 2008).

### 4.4 Host galaxy

We compared the observed host-galaxy SED (Table 3) with a set of spectral synthesis models by using **hyperZ** (see Bolzonella et al. 2000 for details). The lack of measurements redward of the Balmer break at 4000 Å (rest frame) limits our possibility of constraining one of the key parameters, the total stellar mass. We assumed different extinction profiles for modelling the dust extinction produced within the galaxy itself; although the best-fit parameters do not change significantly, we adopted the Calzetti law (Calzetti et al. 2000). The result is shown in Figure 6.

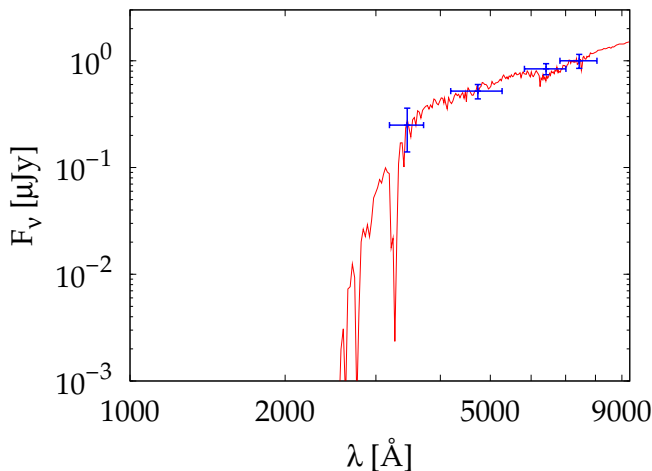
The best-fitting synthetic spectrum belongs to a starburst galaxy with an age of 130 Myr, dust extinction  $A_V = 0.87$  mag, absolute magnitude  $M_B = -20.7$ . By adopting an LMC extinction profile, similar parameters are obtained: 90 Myr age,  $A_V = 0.77$  mag,  $M_B = -20.7$ . These values are typical of other host galaxies of long-duration GRBs (Savaglio et al. 2009; Chen et al. 2009).

## 5 DISCUSSION

GRB 080603A exhibits several interesting properties: (i) the end of the  $\gamma$ -ray prompt emission marked by the simultaneous detection of an optical flash, which appears to be a distinct component from the emerging afterglow following the end of the  $\gamma$ -rays; (ii) an overall achromatic afterglow rise, peak, and decay, followed by a break around  $10^5$  s; (iii) an accurate SED allowing us to precisely measure the remarkable dust content along the sightline to the GRB, clearly

**Table 6.** Spectral energy distribution best-fitting parameters.

Frequency Range ( $10^{15}$ Hz)	Model	Ext. profile	$\beta$	$A_{V,z}$	$N_{\text{H } 1,z}$ ( $10^{21}$ cm $^{-2}$ )	$\nu_{\text{b}}$ ( $10^{17}$ Hz)	$\chi^2/\text{dof}$	Prob (%)
$0.3\text{--}3 \times 10^3$	POW	LMC2	$1.01 \pm 0.05$	$0.80 \pm 0.13$	$6.7^{+2.0}_{-1.8}$	–	19.0/19	46
$0.3\text{--}3 \times 10^3$	POW	SMC	$0.92 \pm 0.04$	$0.48 \pm 0.07$	$5.8^{+1.8}_{-1.6}$	–	39.9/19	0.34
$0.3\text{--}3 \times 10^3$	POW	MW	$1.04 \pm 0.04$	$0.91 \pm 0.12$	$6.5^{+1.9}_{-1.6}$	–	136/19	$< 10^{-15}$
0.3–3	POW	LMC2	$0.8 \pm 0.7$	$0.9^{+0.4}_{-0.3}$	–	–	0.4/4	98
0.3–3	POW	SMC	$2.0^{+0.5}_{-0.6}$	$< 0.33$	–	–	12.1/4	1.7
0.3–3	POW	MW	$2.2^{+0.2}_{-0.4}$	$< 0.28$	–	–	10.5/4	3.3
$200\text{--}3 \times 10^3$	POW	–	$1.3 \pm 0.3$	–	$6.6^{+6.2}_{-4.6}$	–	16.4/13	23
$0.3\text{--}3 \times 10^3$	BKN	LMC2	$0.99 \pm 0.07$	$0.80 \pm 0.13$	$8.0^{+3.2}_{-3.1}$	$8.7^{+4.2}_{-2.7}$	16.6/18	55
$0.3\text{--}3 \times 10^3$	BKN	SMC	$0.89 \pm 0.05$	$0.48 \pm 0.07$	$7.1^{+3.1}_{-1.8}$	$8.2^{+3.8}_{-4.0}$	34.9/18	1.0


**Figure 6.** Observed SED of the host galaxy and the best-fitting synthetic spectrum using hyperZ.

favouring an LMC2 profile at variance with that found for most GRBs. In the following we examine these aspects in the context of the standard afterglow model.

### 5.1 Broadband afterglow modelling

In the context of the standard afterglow model (Mészáros & Rees 1997; Sari et al. 1998; for a review, see, e.g., Mészáros 2006), the power-law piecewise spectra and light curves are interpreted as the result of synchrotron emission of a population of shock-accelerated electrons of a forward shock ploughing into the surrounding medium. The electron energy distribution is assumed to be  $dN/d\gamma \propto \gamma^{-p}$  ( $\gamma > \gamma_m$ ); the values of  $p$  typically derived from GRB afterglow modelling cluster around 2.0–2.4 with a scatter of 0.3–0.5 (Starling et al. 2008; Curran et al. 2010), in general agreement with theoretical expectations (e.g., Achterberg et al. 2001; Spitkovsky 2008).

Following Sari et al. (1998), let  $\nu_m$  and  $\nu_c$  be the synchrotron injection and cooling frequencies, respectively. The observed spectral index  $\beta_{\text{ox}} = 1.0$  (Section 4.2) with no breaks between optical ( $\nu_o$ ) and X-ray ( $\nu_x$ ) frequencies can be explained in two alternative cases:  $\nu_m < \nu_{o,x} < \nu_c$  or  $\max(\nu_m, \nu_c) < \nu_{o,x}$ . In the latter case, the electron index is  $p = 2\beta_{\text{ox}} = 2.0$  (although formally consistent with fast cool-

ing, at late times we can safely assume slow cooling), while in the former case  $p = 2\beta_{\text{ox}} + 1 = 3.0$  (slow cooling).

- $\nu_m < \nu_{o,x} < \nu_c$  ( $p = 3$ ).

The predicted temporal index  $\alpha$  depends on the density profile: either  $\alpha_{\text{ISM}} = 3(p - 1)/4 = 1.5$  (homogeneous or ISM) or  $\alpha_w = (3p - 1)/4 = 2.0$  (wind). Both decay values are significantly steeper than the observed  $\alpha_2 = 1.0$ , respectively, by  $\Delta\alpha_{\text{ISM}} = 0.5$  and  $\Delta\alpha_w = 1.0$ . Even assuming a more general density profile,  $n(r) \propto r^{-s}$ , the expected decay is steeper than ISM for every value of  $s$ . This was also the case for a number of other bursts whose spectral and temporal indices could not fulfil any closure relation (e.g., Melandri et al. 2008). A possible way to explain a shallower decay is energy injection refreshing the blast wave (Rees & Mészáros 1998; Sari & Mészáros 2000; Granot et al. 2003; Melandri et al. 2009), as was also proposed to explain the shallow-decay phase in early X-ray afterglows (Zhang et al. 2006).

Let  $E(t)$  be the fireball energy as a function of the observed time  $t$ , so that  $E(t) \propto t^e$ . Assuming negligible radiative losses, the expected decay index change with respect to no injection,  $\Delta\alpha_{ei}$ , is  $e(p + 3)/4$  (ISM) and  $e(p + 1)/4$  (wind) for  $\nu < \nu_c$  (Panaitescu 2005). The observed values imply  $e = 1/3$  (ISM) and  $e = 1$  (wind). The energy budget may be problematic, as in the afterglow phase from  $10^3$  to  $10^5$  s the required injected energy would be a factor of  $100^{1/3} \approx 5$  (100) larger for ISM (wind). Using the notation of Zhang et al. (2006), these are equivalent to  $q = 2/3$  and  $q = 0$ , respectively, for an injection luminosity  $L(t) \propto t^{-q}$ .

At the end of the injection, the power-law decay is expected to steepen by  $\Delta\alpha_{ei}$  so that the decay should resume the no-injection values,  $\alpha_{\text{ISM}}$  or  $\alpha_w$ . Indeed, the final decay  $\alpha_3 = 1.7^{+0.4}_{-0.3}$  is compatible with both values. In this case, the final break around  $10^5$  s would mark the end of the energy-injection process.

- $\max(\nu_m, \nu_c) < \nu_{o,x}$  ( $p = 2$ ).

Above the cooling frequency the emission does not depend on the ambient density, so for any  $s$  ( $0 < s < 3$ ),  $\alpha = (3p - 2)/4 = 1.0$ . This fully agrees with the observed value of  $\alpha_2$  and there is no need to invoke any additional processes such as energy injection. Another asset of this possibility is that the final power-law decay index,  $\alpha_3 \approx 2$ , nicely supports the jet-break interpretation, being  $\alpha = p$ .

### 5.1.1 Radio afterglow

The peak frequency  $\nu_m$  of the synchrotron spectrum crossed the radio bands between 5 and 12 days: this is suggested by the peak in the light curve at  $\nu_{\text{radio},2} = 8.46$  GHz and by the change in the spectral slope between  $\nu_{\text{radio},1} = 4.86$  GHz and  $\nu_{\text{radio},2}$ . In particular, the slope of the radio spectrum changes from positive to negative: the first 2-channel radio SED at 5 days is fit with  $\beta_{\text{radio}} = -1.3_{-2.0}^{+1.1}$ , while the second SED around 12 days gives  $\beta_{\text{radio}} = 1.8_{-1.6}^{+7.2}$ . At low frequencies the flux is expected to rise as  $t^{1/2}$  and to decay as  $t^{-3(p-1)/4}$  for an ISM (Sari et al. 1998). We fitted the observed 8.46 GHz radio curve under these assumptions in either case considered above (i.e., either  $p = 3$  or  $p = 2$ ) and found the radio peak time  $t_{\text{radio},p} = 4.4_{-0.7}^{+3.7} \times 10^5$  s and the peak normalisation  $F_{\text{radio},p} = 200_{-40}^{+120}$   $\mu\text{Jy}$  from the fit. This could be considerably different, when other temporal behaviours are considered; in particular, a steeper rise followed by a steeper decay could be compatible with  $F_{\text{radio},p} > 200$   $\mu\text{Jy}$ . This possibility is not naturally explained within the standard afterglow model, unless the  $\nu_m$  passage and the jet break happened almost at the same time by chance, implying a  $t^{-p}$  decay.

### 5.1.2 Afterglow onset

The rise experienced by the afterglow in the *BVRi* filters rules out the passage of a typical synchrotron frequency through the observed wavelengths as the possible cause because of both the steepness and the lack of chromatic evolution of the rise itself. The possibility of an afterglow emerging from a wind surrounding a massive progenitor, with the optical rise being due to the progressively decreasing dust extinction (Rykoﬀ et al. 2004), is excluded by the lack of chromatic evolution, as observed in many other cases (e.g., Guidorzi et al. 2009; Krühler et al. 2009).

Here we consider the possibility, discussed in several analogous cases (e.g., Molinari et al. 2007), that the broad optical peak  $t_p = 1575_{-250}^{+430}$  s marks the deceleration of the fireball and the afterglow onset. The duration of the  $\gamma$ -ray burst itself ( $\sim 200$  s) is much shorter than the peak time, as expected in the thin-shell case (Sari 1997). The observed steep rise,  $\alpha_1 = -3.6 \pm 1.7$ , rules out the wind environment for which a shallower rise ( $\sim -0.5$ ) is required. Depending on whether it is  $\nu < \nu_c$  or  $\nu > \nu_c$ , a rise index of  $-3$  or  $-2$  is expected for an ISM (Jin & Fan 2007; Panaitescu & Vestrand 2008), both compatible with observations.

In this context, from the afterglow peak time we can estimate the initial bulk Lorentz factor  $\Gamma_0$  as being approximately twice as large as its value at the peak time (Sari & Piran 1999; Molinari et al. 2007):

$$\Gamma_0 \approx 2 \Gamma(t_p) = 2 \left[ \frac{3E_{\text{iso}}(1+z)^3}{32\pi n m_p c^5 \eta t_p^3} \right]^{1/8} \approx (130 \pm 20) n_0^{-1/8} (3)$$

We assumed standard values for the energy-conversion efficiency,  $\eta_\gamma = 0.2$  and for the particle density of the circumburst environment  $n = n_0 \text{ cm}^{-3}$ . Equation (3) holds for an ISM environment; we do not consider the wind case, because of the incompatible steepness of the rise. Such a bulk Lorentz factor lies within the distribution found for other GRBs (e.g., Liang et al. 2010; Melandri et al. 2010).

Following Zou & Piran (2010), we set an upper limit to

$\Gamma_0$  from the prompt  $\gamma$ -ray light curve, thanks to the presence of a quiescent time between the two pulses. The idea behind this is that while the prompt  $\gamma$ -rays are being produced through internal shocks, the outermost shell begins sweeping up the surrounding medium; as a consequence, a forward shock should appear in soft  $\gamma$ -rays as a smooth and continuously increasing emission. This constraint is only suitable for bursts with a relatively short pulse followed by either a quiescent time or a deep trough, because otherwise the external shock could have significantly decelerated during the first pulse. From Figure 4, at 90 s we estimate a  $3\sigma$  upper limit of 3  $\mu\text{Jy}$  at the mean energy of 84 keV, which corresponds to  $0.3 \times 10^{-28} \text{ erg cm}^{-2} \text{ s}^{-1} \text{ Hz}^{-1}$ . From their Equation (5) we derive the following upper limits to  $\Gamma_0$ :

$$\Gamma_0 < 150 n_0^{-1/8} \epsilon_{e,-1/2}^{-1/5} \epsilon_{B,-1}^{-1/20} (1+Y)^{1/10} \quad (p=3) \quad (4)$$

$$\Gamma_0 < 220 n_0^{-1/8} \epsilon_{e,-1/2}^{-1/8} (1+Y)^{1/8} \quad (p=2.01), \quad (5)$$

where we used  $p = 2.01$  instead of  $p = 2$  as it is applicable only for  $p > 2$ . A value  $p < 2$  would imply electron energy divergence, so a proper formulation is required; this is beyond the scope of the paper.  $\epsilon_B = \epsilon_{B,-1} \times 10^{-1}$  and  $\epsilon_e = \epsilon_{e,-1/2} \times 10^{-1/2}$  are the equipartition factors for the magnetic and the electron energy densities, respectively, and  $Y$  is the Compton parameter for synchrotron self-Compton scattering. These upper limits are remarkably consistent with the estimate derived in Equation (3), especially because a number of GRBs were found to exceed these values.

In the context of peaks interpreted in terms of outflow deceleration and afterglow onset, Panaitescu & Vestrand (2011) proposed that fast-rising optical afterglows are likely caused by an impulsive ejecta release with a narrow distribution of Lorentz factors after the GRB itself, in contrast to an extended release or a broad range of Lorentz factors more suitable to explain the slow-rising/plateau afterglows. The motivation of this interpretation resides in the different correlations between peak time and peak flux found for each class:  $F_p \propto t_p^{-3}$  and  $F_p \propto t_p^{-1/2}$  for fast-rising and plateau afterglows, respectively. Following their guideline, when we move GRB 080603A to a common redshift of  $z = 2$ , its dust-corrected *R*-band peak flux is 0.8 mJy at a peak time of 1750 s (at  $z = 2$ ) — that is, it lies in the region of the  $F_p$ - $t_p$  plane where the two correlations cross each other (see Fig. 1 of Panaitescu & Vestrand 2011). Because of the  $\sim t^3$  rise, GRB 080603A belongs to the peaky afterglow class. Interestingly,  $E_{\text{iso}}$  and  $F_p$  of peaky GRBs are shown to correlate more tightly than those of plateau GRBs; indeed GRB 080603A lies very close to the best-fitting power-law relation shown in Fig. 2 of Panaitescu & Vestrand (2011), in agreement with its being a member of the peaky class. The tighter connection between the  $\gamma$ -ray released energy and the afterglow peak flux for the fast-rising GRBs may support the impulsive ejecta release interpretation.

In the afterglow the presence of a single peak followed by a  $\sim t^{-1}$  decay qualifies GRB 080603A as a Type III member according to the classification by Zhang et al. (2003) and Jin & Fan (2007). At variance with pre-*Swift* expectations mainly based on the case of GRB 990123 (Akerlof et al. 1999), most GRBs show no evidence for a short-lived reverse-shock peak at early times (Mundell et al. 2007; Oates et al. 2009; Rykoﬀ et al. 2009; Kann et al. 2010; Melandri et al. 2010) and GRB 080603A is no exception in

this respect: the prompt optical flash cannot be reverse-shock emission because of the gap between the flash and the afterglow onset. A way to circumvent this problem is that the outer layer of the outflow has much higher Lorentz factor compared to the bulk part of the flow; the outer layer might produce an optical reverse-shock emission well before the onset of the afterglow, which is determined by the main part of the flow. However, the rather narrow spike seems to disfavour this model. Among the possible explanations, such as either a high or a low magnetic energy density in the ejecta (e.g., Gomboc et al. 2008), here we consider the low-frequency model (Melandri et al. 2010): at the shock-crossing time, marked by the peak, both injection frequencies of forward and reverse shocks,  $\nu_{m,f}$  and  $\nu_{m,r}$  (respectively), lie below the optical band (Mundell et al. 2007).

Assuming the same microphysical parameters in both shocks, the relation between the spectral characteristics of the shocks at  $t = t_p$  are

$$\frac{\nu_{m,r}}{\nu_{m,f}} \approx \Gamma^{-2}, \quad \nu_{c,r} \approx \nu_{c,f}, \quad \frac{F_{\max,r}}{F_{\max,f}} \approx \Gamma, \quad (6)$$

where  $F_{\max}$  is the peak flux in the frequency domain at a given time, in this case at  $t_p$ , different from the peak flux in the time domain at a given frequency, denoted with  $F_p$ . We discuss the implications in the two cases considered above.

- $\nu_m < \nu_{o,x} < \nu_c$  ( $p = 3$ ).

This requires  $\nu_{m,f} \lesssim \nu_o$  and  $\nu_c > \nu_x$  at  $t = t_p$ , where  $\nu_o = 5 \times 10^{14}$  Hz and  $\nu_x = 10^{18}$  Hz. As discussed above, the observed temporal decay requires energy injection with  $q = 2/3$  up to the late-time break. Temporal evolution of the characteristic frequencies and peak of the forward shock is  $\nu_{m,f} \propto t^{-(q+2)/2} = t^{-4/3}$ ,  $\nu_c \propto t^{(q-2)/2} = t^{-2/3}$ , and  $F_{\max,f} \propto t^{1-q} = t^{1/3}$  (Zhang et al. 2006). Interpreting the radio flux at  $t_{\text{radio}} = 4.1 \times 10^5$  s as mostly due to the forward shock, using the result of the corresponding SED fitting discussed in Section 4.2 and shown in Figure 7 (dashed-dotted line), we can estimate the time at which  $\nu_{m,f}$  crossed the optical bands:  $t_{\text{radio}} (\nu_o/\nu_{m,f}(t_{\text{radio}}))^{-3/4} (t_{\text{radio}}/t_{b2})^{1/8} = 7 \times 10^3$  s. This is derived from the temporal dependence of  $\nu_{m,f} \propto t^{-4/3}$  as long as energy injection goes on (so for  $t < t_{b2}$ ), and  $\nu_{m,f} \propto t^{-3/2}$  (for  $t > t_{b2}$ ). The absence of any break or spectral evolution in the multi-filter light curve of Figure 4 rules out any such passage at this time. Even worse, as discussed in Section 4.2, the derived value of  $\nu_{m,f}$  from Figure 7 is incompatible with its passage through the radio bands at  $t_{\text{radio},p}$  as observed from the radio curve (Section 5.1.1), because it implies a too rapid decay of  $\nu_{m,f}$ .

The expected contribution to the radio flux from the reverse shock exceeds the observed values by a factor of  $10^2$ : at the peak time,  $F_{\max,r} \approx 80$  mJy. This is found from Equation (6) and from  $F_{\max,f} \approx F_{p,\text{unext}} = 1200$   $\mu$ Jy, where we used the observed flux density in the  $R$  band at the peak time,  $F_p = 180 \pm 6$   $\mu$ Jy; removing the intrinsic dust extinction of  $A_{V,z} = 0.8$  mag, the unextinguished value is  $F_{p,\text{unext}} = 1200$   $\mu$ Jy. From the deceleration time to the end of the energy injection, it is  $F_{\max,r} \approx F_{\max,f} \Gamma \propto t^{1-q-(2+q)/8} = t^0$  (Table 7 and Zhang et al. 2006). From that time to  $t_{\text{radio}}$ , it is  $F_{\max,r} \propto t^{-1}$  (Kobayashi 2000; Zhang et al. 2003). It is therefore  $F_{\max,r}(t_{\text{radio}}) = 80 (t_{\text{radio}}/t_{b2})^{-1} \approx 20$  mJy. From Equation (6)  $\nu_{m,r} \approx \nu_o/\Gamma^2 = 1.2 \times 10^{11}$  Hz at the peak time. Using the temporal scaling of  $\nu_{m,r}$ , its value at  $t_{\text{radio}}$  is found to be

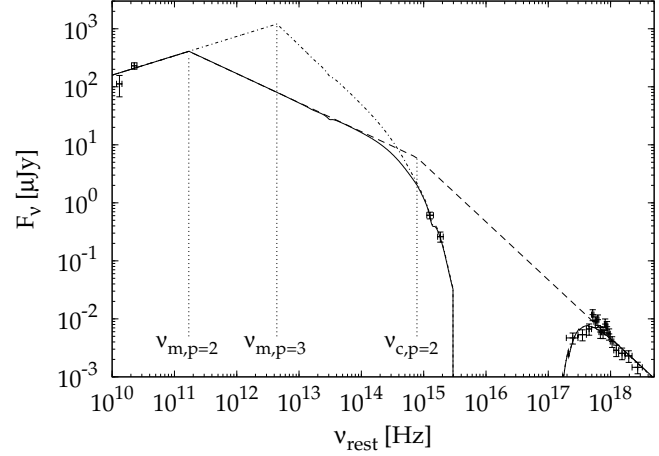


**Figure 7.** Rest-frame spectral energy distribution at  $4.1 \times 10^5$  s. Two alternative models are shown, depending on whether  $\nu_c$  lies below the optical ( $p = 2$ ; solid line) or above X-rays ( $p = 3$ ; dashed-dotted line). Characteristic frequencies are reported. Both models are extinguished with an LMC2 dust profile. The dashed line is the same as the solid line, removed of dust extinction.

$\nu_{m,r}(t_{\text{radio}}) = \nu_{m,r}(t_{b2}/t_p)^{-2/3} (t_{\text{radio}}/t_{b2})^{-3/2} \approx 1$  GHz, where we used  $\nu_{m,r} \propto t^{-2/3}$  for  $t < t_{b2}$  (Table 7) and  $\nu_{m,r} \propto t^{-3/2}$  for  $t > t_{b2}$  (Kobayashi 2000). This means that around the time of observations,  $\nu_{m,r}$  should have crossed the radio band. The expected flux should therefore be comparable with  $F_{\max,r}(t_{\text{radio}}) \approx 20$  mJy. Although the passage of the peak synchrotron (of the reverse shock) through the radio band is indeed compatible with the radio light curve, the observed flux is about two orders of magnitude smaller than expected. Although in principle self-absorption could explain this, in the following we show that here it appears unlikely. Another possibility to suppress the reverse-shock radio emission at late times is assuming a hot flow (i.e., Poynting-flux dominated).

Equation (6) is valid as long as we consider energy injection to the shock by a cold flow (i.e., injection of kinetic energy). More generally, assuming the same velocity and pressure in the FS and RS regions, the ratio  $F_{\max,r}/F_{\max,f}$  is proportional to the corresponding ratio of the number of electrons in the two shock regions. Considering an extreme case of no new electron injection in the reverse-shock region, it is  $F_{\max,r}/F_{\max,f} \approx N_{e,r}/N_{e,f} \sim r^{-3} \approx t^{-3(2-q)/4} = t^{-1}$ . Similarly,  $\nu_{m,r}/\nu_{m,f} \approx (\gamma_{e,r}/\gamma_{e,f})^2 \approx (\rho_f/\rho_r)^2 \approx r^6 \approx t^{3(2-q)/2} = t^2$ ;  $\nu_{c,r} \approx \nu_{c,f} \approx t^{(q-2)/2} \approx t^{-2/3}$ . These might be more uncertain compared to the cold-flow results, where we have assumed that the FS and RS regions have comparable widths.

- $\max(\nu_m, \nu_c) < \nu_{o,x}$  ( $p = 2$ ).

This requires  $\nu_{m,f} \lesssim \nu_o$  and  $\nu_c \lesssim \nu_o$  at  $t = t_p$ . No energy injection is required to explain the spectral and temporal properties of the afterglow. The characteristic synchrotron frequencies can be expressed by (Sari et al. 1998; Kobayashi & Zhang 2003a)

$$\nu_c(t_p) \approx 6.8 \times 10^{12} \epsilon_B^{-3/2} E_{52}^{-1/2} \eta_{0.2}^{1/2} n_0^{-1} \zeta^{-1/2} t_{p,3}^{-1/2} \text{ Hz}, \quad (7)$$

$$\nu_{m,f}(t_p) \approx 1.7 \times 10^{18} \epsilon_B^{1/2} \epsilon_e^2 E_{52}^{1/2} \eta_{0.2}^{-1/2} \zeta^{1/2} t_{p,3}^{-3/2} \text{ Hz}, \quad (8)$$

where  $\eta_{0.2} = \eta/0.2$ ,  $t_{p,3} = t_p/10^3$  s,  $E_{52} = E_{\text{iso}}/10^{52}$  erg, and  $\zeta = (1+z)/2.687$ . In particular, it is  $\nu_c \approx 3.6 \times$

Shock	$L \propto t^{-q}$			$E(> \gamma) \propto \gamma^{-s+1}$		
	$\nu_m$	$\nu_c$	$F_{\max}$	$\nu_m$	$\nu_c$	$F_{\max}$
FS	$-(q+2)/2$	$(q-2)/2$	$(1-q)$	$-12/(7+s)$	$-2(s+1)/(7+s)$	$3(s-1)/2(7+s)$
RS	$-(q+2)/4$	$(q-2)/2$	$3(2-3q)/8$	$-6/(7+s)$	$-2(s+1)/(7+s)$	$3(s-2)/2(7+s)$

**Table 7.** Temporal exponent of injection and cooling frequencies, as well as of the maximum flux density for the forward shock (FS) and the reverse shock (RS) in the case of continuous energy injection through an ISM. The two formalisms, the luminosity as a function of time on the left-hand side, and the energy distribution of the shells as a function of the bulk Lorentz factor on the right-hand side, are equivalent (Sari & Mészáros 2000; Zhang et al. 2006). The two parameters  $q$  and  $s$  are related by  $s = (10 - 7q)/(q + 2)$  and  $q = (10 - 2s)/(7 + s)$ . The impulsive case (i.e., no continuous injection) corresponds to  $s = q = 1$ .

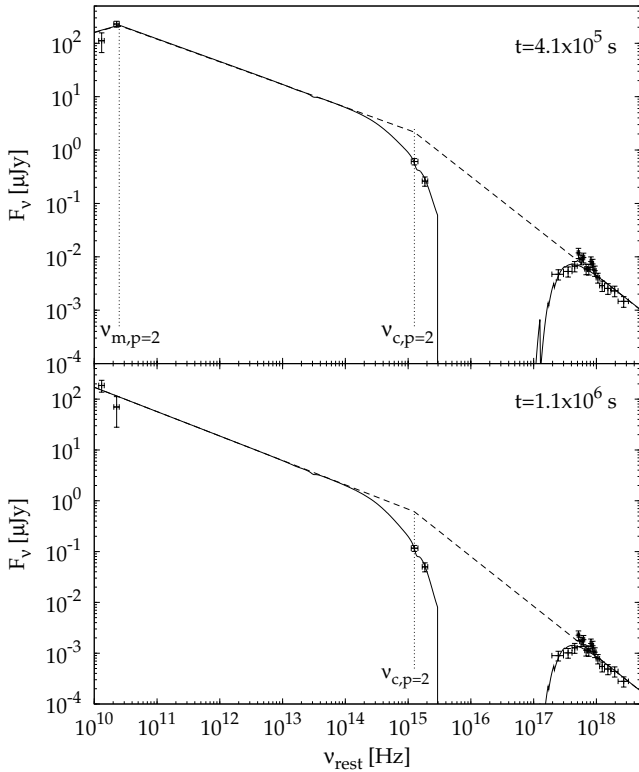


**Figure 8.** *Top panel:* rest-frame SED at  $4.1 \times 10^5$  s. The solid line shows the synchrotron spectrum with an LMC2 dust-extinction profile for the  $p = 2$  case. The corresponding injection and cooling frequencies are indicated. The dashed line shows the same unextinguished model. *Bottom panel:* rest-frame SED at  $1.1 \times 10^6$  s. The data are consistent with being taken after the passage of  $\nu_m$  through the radio band.

$$10^{12} \epsilon_B^{-3/2} n_0^{-1} \text{ Hz}, \nu_{m,f} \approx 1.3 \times 10^{18} \epsilon_B^{1/2} \epsilon_e^2 \text{ Hz}, \text{ and } \nu_{m,r} \approx 3 \times 10^{14} \epsilon_B^{1/2} \epsilon_e^2 \text{ Hz}.$$

The requirements on the characteristic frequencies at the peak time become  $\epsilon_B^{1/2} \epsilon_e^2 \lesssim 4 \times 10^{-4}$  and  $\epsilon_B^{-3/2} n_0^{-1} \lesssim 140$ . A possible solution is  $\epsilon_B \approx 10^{-2}$ ,  $\epsilon_e \approx 3 \times 10^{-2}$ ,  $n_0 \approx 10$ , which gives  $\nu_c \approx 3.6 \times 10^{14}$  Hz and  $\nu_{m,f} \approx 1.2 \times 10^{14}$  Hz. The much lower  $\nu_c$  than the previous case would be mainly due to a denser environment.

The expected peak flux of the forward shock at the peak frequency  $\nu_{m,f}$  is then  $F_{\max,f}(t_p) \approx (\nu_{m,f}/\nu_c)^{-(p-1)/2} (\nu_c/\nu_o)^{-p/2} F_{p,\text{next}} \approx 3$  mJy. The contribution of the reverse shock to the optical peak luminosity in the  $R$  band is comparable: from Equation (6)

the reverse shock peaks at  $\nu_{m,r} \approx \nu_{m,f}/\Gamma^2 \approx 2.4 \times 10^{10}$  Hz with  $F_{\max,r} \approx \Gamma F_{\max,f}$  which scales at  $\nu_{m,f}$  by the factor  $(\nu_{m,f}/\nu_{m,r})^{-(p-1)/2} = \Gamma^{-1}$ . The net result is  $F_r(\nu_{m,f}) \approx F_f(\nu_{m,f})$ .

At  $t = t_{\text{radio}}$ , the expected luminosity is dominated by the forward shock. From the frequency and flux-density scalings  $\nu_{m,f} \propto t^{-3/2}$ ,  $\nu_{c,f} \propto t^{-1/2}$ ,  $F_{\max,f} \propto t^0$ ,  $\nu_{m,r} \propto t^{-3/2}$ ,  $\nu_{c,r} \propto t^{-3/2}$ , and  $F_{\max,r} \propto t^{-1}$  (Zhang et al. 2003; Mundell et al. 2007), we have  $\nu_{m,f}(t_{\text{radio}}) \approx 3 \times 10^{10}$  Hz,  $\nu_{m,r}(t_{\text{radio}}) \approx 7 \times 10^6$  Hz. This means that the peak of the reverse shock has already crossed the radio band, while that of the forward shock has not yet. The two expected flux densities at 8.46 GHz are  $F_f(t_{\text{radio}}) \approx 3(\nu_{\text{radio}}/\nu_{m,f}(t_{\text{radio}}))^{1/3} \approx 2$  mJy and  $F_r(t_{\text{radio}}) \approx 3(\nu_{\text{radio}}/\nu_{m,r}(t_{\text{radio}}))^{-(p-1)/2} (t_{\text{radio}}/t_p)^{-1}$  mJy  $\approx 0.3$   $\mu$ Jy, respectively. Thus, given that the expected flux from the reverse shock is 3 orders of magnitude smaller than observed, while that of the forward shock differs by a factor of few, hereafter we focus on the latter.

The solid line of Figure 7 shows the result of fitting the broadband SED at  $t_{\text{radio}}$  with both  $\nu_{m,f}$  and  $\nu_{c,f}$  below the optical and having fixed  $p = 2$  and the rest-frame dust extinction. The free parameters are the break frequencies as well as the normalisation. We found  $\nu_{m,f}(1+z) = 1.7_{-0.8}^{+93} \times 10^{11}$  Hz and  $\nu_{c,f}(1+z) = 8_{-3}^{+5} \times 10^{14}$  Hz ( $\chi^2/\text{dof} = 20.9/17$ ). Not only does the value for  $\nu_{m,f}$  agree with expectations, but also the peak flux of  $\sim 400$   $\mu$ Jy resulting from the fit is nearly compatible with the value derived from the radio light curve (Section 5.1.1). The downside is the value for  $\nu_{c,f}$ : being so close to the optical band, it must have crossed it at some time  $t \lesssim t_{\text{radio}}$ . This would imply  $\beta_o = (p-1)/2 = 0.5$  for  $t < t_{\text{radio}}$ , which is clearly not true. A possible solution could be to assume a cooling frequency that increases with time, but given that we ruled out a wind environment, this option is not acceptable either. Another problem concerns the crossing time of  $\nu_{c,f}$  through the radio band, observed immediately afterward at  $t_{\text{radio,p}} \approx 1.1 t_{\text{radio}}$  (Section 5.1.1).

We tried to decrease the latter problem by fixing  $\nu_{m,f}$  to the value expected from the time it crossed the radio band — that is, by imposing  $\nu_{m,f} = \nu_{\text{radio}} (t_{\text{radio}}/t_{\text{radio,p}})^{-3/2} = 9.4$  GHz. We allowed all the remaining parameters to vary. The result is shown in the top panel of Figure 8. The best-fitting parameters are  $\nu_{c,f}(1+z) = (1.3 \pm 0.1) \times 10^{15}$  Hz,  $\beta_{\text{ox}} = 0.92 \pm 0.04$  and  $A_{V,z} = 0.56 \pm 0.10$  mag. Although the spectral index is slightly harder than that found at previous epochs, both the normalisation and the slope of the radio-to-optical spectrum fit in the expected broadband modelling well. This explains both the spectrum and light curve of the radio observations. The bottom panel of Figure 8 shows the

SED at  $t = 1.1 \times 10^6$  s, when  $\nu_{m,f}$  has just crossed the radio band. Apart from the same issue with  $\nu_{c,f}$  already mentioned, this is in remarkable agreement with expectations:  $\nu_{c,f}(1+z) = (1.3 \pm 0.1) \times 10^{15}$  Hz,  $\beta_{\text{ox}} = 0.98 \pm 0.05$ , and  $A_{V,z} = 0.72 \pm 0.10$  mag. Yet, the inferred temporal evolution of the cooling frequency remains an issue. In this case, this would lie within the optical bands and the aforementioned argument still applies.

Overall, the  $p = 2$  case works better than  $p = 3$  and can account for more observed properties of the broadband afterglow evolution. Still, the derived evolution of the cooling frequency with time conflicts with a homogeneous environment, the only one compatible with the data.

### 5.1.3 Self-absorption

So far we assumed a negligible effect due to self-absorption in the observed radio flux. Should the radio flux be self-absorbed, from Figure 7 both cases could be compatible with having a high value of  $F_{\text{max}}$ . In particular, for the  $p = 2$  case the temporal evolution of  $\nu_{c,f}$  would no longer be an issue, because it could lie well below  $\nu_o$  at  $t = t_{\text{radio}}$ . To significantly suppress the radio flux, one should require  $\nu_c \ll \nu_o$  already at the peak time; however, this would imply a much larger optical luminosity and an unusually high energy budget. This seems very unlikely, given that the optical luminosity of GRB 080603A, corrected for the dust extinction, already lies in the mid-to-bright end of the observed optical afterglow distribution (Section 5.3 and Figure 11).

Although at lower frequencies and early times self-absorption can significantly suppress the flux, this does not explain these observations unless one makes extreme assumptions. A simple estimate of the maximum flux is that of a black body with the forward-shock temperature (Sari & Piran 1999; Kobayashi & Sari 2000; Mundell et al. 2007), which at the peak time in the optical ( $t = t_p$ ) is given by

$$F_{\nu, \text{BB}}(t_p) \approx \pi(1+z)\nu^2 \epsilon_e m_p \Gamma^2 \left(\frac{R_{\perp}}{D_L}\right)^2 \quad (9)$$

$$\approx 500 \left(\frac{\nu}{\nu_{\text{radio}}}\right)^2 \epsilon_{e,-2} n_0^{-1/2} \mu\text{Jy}, \quad (10)$$

where  $R_{\perp} \approx 4.6\Gamma ct_p$  is the observed fireball size and the dependence on  $n_0$  is inherited from Equation (3). The value derived from Equation (10) initially increases as  $\sim t^{1/2}$ , and steepens to  $\sim t^{5/4}$  after  $\nu_{m,f}$  crosses the observed frequency; thus, at the time of radio observations the black-body flux-density limit expressed by Equation (10) increases by a factor of  $\sim 20$ . This can hardly explain the observed radio flux unless one assumes  $\epsilon_e \approx 10^{-4}$  and/or a high-density environment ( $n \approx 400 \text{ cm}^{-3}$ ). This value for  $\epsilon_e$  would imply that  $\nu_m$  is much below the optical bands ( $\nu_{m,f} \approx 10^{8.5-9}$  Hz) at the peak time and, consequently, an unreasonably high value for  $F_{\text{max},f}$ .

### 5.1.4 Off-axis jet

In the off-axis jet interpretation, the afterglow rise and peak do not mark the fireball deceleration, but are the result of a geometric effect due to an observer angle,  $\theta_{\text{obs}}$ , being larger than the jet opening angle,  $\theta_j$ : as the jet decelerates, the

relativistic beaming angle  $1/\Gamma$  progressively increases, resulting in a rising light curve as seen from the off-axis observer, provided that the jet structure is such that the energy and  $\Gamma$  drop sharply at  $\theta > \theta_j$ . The peak is reached when  $\Gamma(\theta_{\text{obs}} - \theta_j) \approx 1$ , as the sightline enters the beaming cone at the edge of the jet; finally, the decay asymptotically approaches the light curve for an on-axis observer (Granot et al. 2005).

We can estimate  $\theta_{\text{obs}}$  from the peak time as follows:  $\theta_{\text{obs}} - \theta_j \approx 1/\Gamma(t_p)$ . Interpreting the late-time break as being due to the jet, it is  $\theta_j \approx 1/\Gamma(t_j)$ , from which we estimated  $\theta_j \approx 5^\circ.7$  (Section 5.3). Assuming that the deceleration of the jet occurs before the peak, we can assume the temporal scaling of the bulk Lorentz factor as  $\Gamma \propto t^{-3/8}$  for an adiabatic cooling (Rees & Mészáros 1992):

$$\frac{\theta_{\text{obs}} - \theta_j}{\theta_j} \approx \frac{\Gamma(t_j)}{\Gamma(t_p)} \approx \left(\frac{t_j}{t_p}\right)^{-3/8} \approx 0.2, \quad (11)$$

so  $(\theta_{\text{obs}} - \theta_j) \approx 1^\circ$ .

Given the steep rise observed for GRB 080603A, we conveniently consider the case of a sharp-edged, homogeneous jet seen at  $\theta_{\text{obs}} > \theta_j$ . The observed peak energy of the prompt emission,  $E_p$ , falls off as  $b^2$ , where  $b = \Gamma(\theta_{\text{obs}} - \theta_j)$ , while the observed energy falls off rapidly as  $b^6$  (Granot et al. 2002). From Equation (11),  $b \approx 2\Gamma_{100}$ , implying the following on-axis values:  $E_p(\theta_{\text{obs}} = 0) \approx 600\Gamma_{100}^2$  keV and, and  $E_{\text{iso}}(\theta_{\text{obs}} = 0) \approx 10^{54}\Gamma_{100}^6$  erg; here,  $\Gamma$  is the initial value of the bulk Lorentz factor. These estimates are only illustrative and show that, in principle, this scenario could work for reasonable values of the physical parameters in the case of a uniform sharp-edged jet.

However, more realistically the jet cannot be exactly uniform with very sharp edges; in particular,  $\Gamma$  is expected to be lower at the edge and higher at the jet core. Hydrodynamic simulations have shown that, particularly for  $1 \lesssim \theta_{\text{obs}}/\theta_j \lesssim 2$ , very shallow rises or decays of the early-afterglow light curves are expected for realistic jet structure and dynamics (Granot et al. 2002; Eichler & Granot 2006).

Alternatively, structured jets (Zhang & Mészáros 2002) with most of the energy concentrated in the core can reproduce steep rises in the light curves (Kumar & Granot 2003; Granot et al. 2005; Eichler & Granot 2006).

Following Panaitescu & Vestrand (2008), assuming an angular profile for energy as  $\mathcal{E}(\theta) \propto (\theta/\theta_j)^{-q}$ , a  $\sim t^3$  rise would be obtained for  $q = 4$  and  $\theta_{\text{obs}}/\theta_j \approx 1.5 \div 2.5$ . GRB 080603A lies within the  $1\sigma$  region of the correlation between peak time and peak flux for fast-rising afterglows, also discussed by Panaitescu & Vestrand (2011) (Section 5.1.2; see Fig. 2 of Panaitescu & Vestrand 2008).

The scenario of a viewing angle slightly larger than the jet angle seems to be consistent with the nature of a typical GRB, in contrast to the classes of spectrally softer events, such as the so-called X-ray rich GRBs (XRRs) or X-ray flashes (XRFs; e.g., Sakamoto et al. 2008 and references therein). Larger viewing angles are expected to be associated with softer observed events (Yamazaki et al. 2002; Granot et al. 2002; Granot et al. 2005), and the off-axis interpretation for events of this type appears to be favoured (e.g., Guidorzi et al. 2009). In this context, GRB 080603A could represent a soft/intermediate classical GRB with a typical jet opening angle and viewed with a comparable viewing angle.



## 5.2 Prompt optical/ $\gamma$ -ray emission: inverse Compton?

Before the onset of the afterglow marked by the steep rise at the end of the  $\gamma$ -ray prompt emission, the optical flux detected simultaneously with the second and last  $\gamma$ -ray pulse is unlikely to be synchrotron radiation of the shocked ISM. As noted in Section 4.3, the spectral index measured during the prompt emission in the  $\gamma$ -ray band is likely to be an intermediate value between the typical low-energy and high-energy photon indices of a Band function. In this respect, the optical emission could be consistent with the extrapolation of the  $\gamma$ -ray spectrum down to the optical band. A cross-correlation study between the optical and  $\gamma$ -ray profiles would certainly settle this issue; however, in practice this is not possible because of the coarse optical coverage, which gave only three points separated by gaps in between (Fig. 1).

The variety of observed behaviours in other GRBs is rich: the prompt optical was observed to be uncorrelated with the ongoing high-energy emission for GRB 990123 (Akerlof et al. 1999) (e.g., see also GRB 060111B, Klotz et al. 2006; Stratta et al. 2009; GRB 080607, Perley et al. 2011), whereas a strong correlation was observed, for example, for GRB 050820A (Vestrand et al. 2006), superposed on the onset of the afterglow (Cenko et al. 2006). Similar cases of some degree of correlation between the  $\gamma$ -ray prompt and optical emissions are GRB 041219A (Vestrand et al. 2005; Blake et al. 2005), GRB 060526 (Thöne et al. 2010), and GRB 080319B (Racusin et al. 2008; Beskin et al. 2010). One of the most common cases is that the prompt optical observations, typically starting during the final part of the  $\gamma$ -ray emission, suggest the transition from the inner-engine activity to the multi-band afterglow onset; see, for instance, GRB 051111 (Yost et al. 2007), GRB 081008 (Yuan et al. 2010), GRB 081126 (Klotz et al. 2009), and GRB 080928 (Rossi et al. 2011). In one case, a strong optical flare incompatible with an external-shock origin was observed before the afterglow onset (Greiner et al. 2009). In some other cases, the optical profile is dominated by the onset of the external shock of the ejecta through the ISM (e.g., GRB 080810, Page et al. 2009; GRB 061007, Rykoff et al. 2009; Mundell et al. 2007).

Evidence has also been reported for a sizable temporal lag of a few seconds between the optical and high-energy profiles (Klotz et al. 2009; Rossi et al. 2011; Beskin et al. 2010). This potentially represents a strong clue to explain the prompt-emission mechanism.

Comparison of the optical and  $\gamma$ -ray fluxes is also useful for establishing the possible link: while some GRBs have an optical-to- $\gamma$  spectral index  $\beta_{\text{opt}-\gamma}$  compatible with  $\beta_\gamma$ , as can be the case for GRB 080603A, other events show an excess of optical emission with respect to the extrapolation of the high-energy spectrum: up to  $10^4$  times larger, as in the case of GRB 080319B (Racusin et al. 2008). By contrast, there are also cases in which the optical flux lies below the high-energy spectrum extrapolation, such as GRB 050401 (Rykoff et al. 2005; Yost et al. 2007). The latter situation does not necessarily imply different origins or mechanisms for optical and high-energy emissions, but could merely be due to either dust extinction (as is at least partially the

case for GRB 050401, Kann et al. 2010) or a synchrotron spectrum peaking between the two energy ranges.

GRB 080603A is an example where both components (internal activity and afterglow onset) are clearly temporally separated. Although no firm conclusion can be drawn on the possible existence of a temporal lag between optical and  $\gamma$ -ray photons, this GRB resembles GRB 081126 (Klotz et al. 2009): both  $\gamma$ -ray profiles consist of two disjoint FRED-like pulses, the last of which is observed simultaneously with an optical flash, followed by the afterglow onset.

Following Piran et al. (2009), we tested whether the  $\gamma$ -ray prompt emission of GRB 080603A can be explained in terms of an IC process by a population of relativistic electrons on low-energy seed photons. The same electrons would also upscatter the  $\gamma$ -ray photons to GeV–TeV energies. To avoid the energy crisis (i.e., when most of the energy is released in the GeV–TeV range owing to a large  $Y$  parameter), we used the simultaneous optical and  $\gamma$ -ray flux densities to constrain the bulk Lorentz factor  $\Gamma$ . Let  $\gamma_e$  be the Lorentz factor of electrons within the fluid rest frame,  $\nu_L$  the (GRB rest-frame) peak frequency of the lower spectral component (i.e., of the seed  $\nu F_\nu$  spectrum), and  $F_L$  the corresponding peak flux. Also, let  $\nu_{\text{opt}} = \nu_o (1+z) = 1.34 \times 10^{15}$  Hz be the rest-frame frequency corresponding to the observed optical band.  $F_L$  can then be expressed as

$$F_L = (\nu_L/\nu_{\text{opt}})^{-\beta} F_{\text{opt}}, \quad (12)$$

where  $F_{\text{opt}} = 160 \mu\text{Jy}$  is the unextinguished flux of the optical flash. Two possible cases are considered: for the UV (IR) solution, corresponding to  $\nu_L > \nu_{\text{opt}}$  ( $\nu_L < \nu_{\text{opt}}$ ), we assume three possible values for the spectral index:  $\beta = 0$ ,  $-0.5$ , and  $-1$  ( $\beta = 1, 1.5$ , and  $2$ ). The Compton parameter  $Y_L$  in the first IC scattering is

$$Y_L = \left( \frac{\nu_\gamma F_\gamma}{\nu_{\text{opt}} F_{\text{opt}}} \right) \left( \frac{\nu_L}{\nu_{\text{opt}}} \right)^{-(1-\beta)} \approx 10^4 \left( \frac{\nu_L}{\nu_{\text{opt}}} \right)^{-(1-\beta)}, \quad (13)$$

where  $h\nu_\gamma = 84(1+z) = 226$  keV and  $F_\gamma = 41 \mu\text{Jy}$  (Table 1). The first-order IC scattering is not in the Klein-Nishina (KN) regime, so it is  $\nu_\gamma/\nu_L = \gamma_e^2$ , or, equivalently,

$$\gamma_e = \left( \frac{\nu_\gamma}{\nu_{\text{opt}}} \right)^{1/2} \left( \frac{\nu_{\text{opt}}}{\nu_L} \right)^{1/2} = 200 \left( \frac{\nu_{\text{opt}}}{\nu_L} \right)^{1/2}. \quad (14)$$

The second-order IC scattering might be in the KN regime, so  $Y_H$  is

$$Y_H = \left( \frac{\nu_\gamma F_\gamma}{\nu_{\text{opt}} F_{\text{opt}}} \right) \left( \frac{\nu_L}{\nu_{\text{opt}}} \right)^{-(1-\beta)} \min(1, \xi^{-2}), \quad (15)$$

where  $\xi = (\gamma_e/\Gamma) h\nu_\gamma/m_e c^2$  is the correction factor in the KN regime. The energy of the upscattered photons is

$$h\nu_H = 9 \text{ GeV} \left( \frac{\gamma_e}{200} \right)^2 \min\left(1, \frac{\Gamma m_e c^2}{\gamma_e h\nu_\gamma}\right), \quad (16)$$

and the corresponding Compton parameter  $Y_H$  is

$$Y_H = 10^4 \left( \frac{\nu_L}{\nu_{\text{opt}}} \right)^{-(1-\beta)} \min\left[1, \left( \frac{\Gamma m_e c^2}{\gamma_e h\nu_\gamma} \right)^2\right]. \quad (17)$$

The energy-crisis problem mainly resides in the large value for  $Y_H$ . Figure 9 shows  $Y_H$  as a function of  $\nu_L$  for the values of the spectral index considered above and assuming for  $\Gamma$  the value we derived in Equation (3). There are two solutions for which the released energy is not an issue: the UV solution requires  $\beta \leq -1$  and  $\nu_L > 30 \nu_{\text{opt}}$ , equivalent

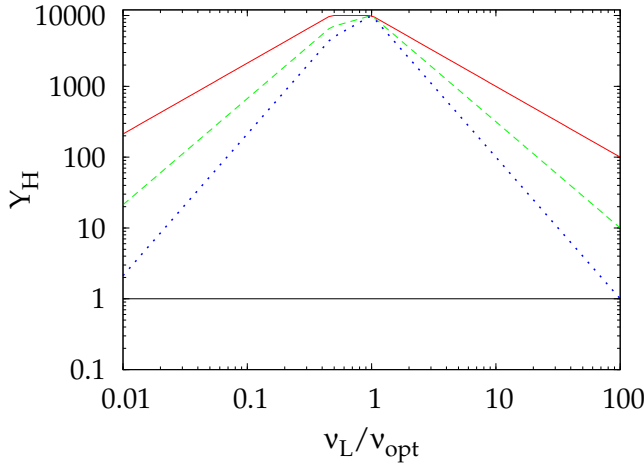


**Figure 9.**  $Y_H$  as a function of  $\nu_L/\nu_{\text{opt}}$  for  $\Gamma = 130$  and (from top to bottom)  $\beta = 0, -0.5,$  and  $-1$  for  $\nu_L > \nu_{\text{opt}}$ , and (from top to bottom)  $\beta = 1, 1.5, 2$  for  $\nu_L < \nu_{\text{opt}}$  (adapted from Piran et al. 2009).

to  $\gamma_e < 37$  (Eq. (14)). This solution is characterised by a negligible KN suppression. The total energy is at least  $3 E_\gamma$ , given that  $Y_H \approx Y_L$ . Other problems with the UV solutions are (i) a low efficiency due to the low  $\gamma_e$ , because protons would carry at least a factor of  $m_p/\gamma_e m_e$  more energy than electrons, unless one requires pair loading; and (ii) at such low values of  $\gamma_e$ ,  $\nu_L$  increases and its flux  $F_L$  is limited not only by  $F_{\text{opt}}$ , but also by the prompt soft X-ray observations. Whenever available, these data rule out the UV solution (Piran et al. 2009). Although for GRB 080603A there are no prompt X-ray observations, the UV solution appears contrived.

The IR solution requires  $\beta \geq 2$  and  $\nu_L \lesssim 0.01 \nu_{\text{opt}}$ , equivalent to  $\gamma_e \gtrsim 2000$ . This solution is characterised by a high value for  $Y_L$ , and a relatively small value for  $Y_H$ , because of the KN suppression. This becomes important for  $\nu_L < 0.46 \nu_{\text{opt}}$ , as shown by the break in Figure 9. On the other hand, for very low  $\nu_L/\nu_{\text{opt}}$  the expected  $F_L$  also increases for a given  $F_{\text{opt}}$  and self-absorption can represent an issue. To avoid this, one has to require  $F_{\text{sa}}(\nu_L) > F_L$ , where  $F_{\text{sa}}(\nu_L)$  is the black-body flux for a local temperature  $kT \approx \Gamma \gamma_e m_e c^2$ ,

$$F_{\text{sa}}(\nu_L) = \frac{2\nu_L^2}{c^2} \gamma_e m_e c^2 \frac{R^2}{4\Gamma d_L^2}, \quad (18)$$

where  $R$  is the radius of the source and  $d_L = 12.74$  Gpc is the luminosity distance of GRB 080603A. From this requirement on  $F_L$  we can constrain  $\Gamma$  for  $\nu_L < \nu_{\text{opt}}$ :

$$\Gamma < \frac{1}{2} \left( \frac{R}{d_L} \right)^2 \nu_\gamma^{2+\beta} \frac{\nu_{\text{opt}}^{-\beta}}{F_{\text{opt}}} m_e \gamma_e^{-(2\beta+3)}. \quad (19)$$

We conservatively assume  $R = 10^{17}$  cm. The corresponding allowed  $\Gamma$ - $\gamma_e$  phase space is shown in Figure 10 in the IR-solution domain, enclosed by the decreasing curves on the right-hand side. Combining this with the  $Y_H \leq 1$  regions and with the corresponding values for the spectral index shows that the value measured for  $\Gamma$  in Equation (3) does not overlap with any total allowed region (darkest areas).

We conclude that the prompt optical and  $\gamma$ -ray data are not compatible with an IC origin for the latter as a result of

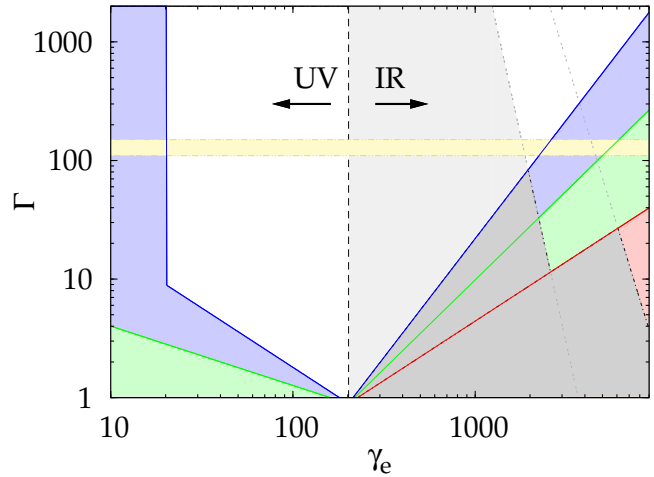


**Figure 10.** The allowed (shaded) phase space characterised by  $Y_H \leq 1$  (from bottom to top) for  $\beta = 0, -0.5,$  and  $-1$  for  $\nu_L > \nu_{\text{opt}}$  and (from bottom to top)  $\beta = 1, 1.5, 2$  for  $\nu_L < \nu_{\text{opt}}$ . The two decreasing functions in the IR solution mark the self-absorption limits for  $\beta = 2$  (grey area; lower  $\gamma_e$  range) and  $\beta = 1$  (higher  $\gamma_e$  range), respectively. The two darkest areas partially overlapping each other are the intersection of the allowed regions for  $\beta = 2$  and for  $\beta = 1$ , respectively. The interval  $\Gamma = 130 \pm 20$  (estimated from the peak in the afterglow light curve) is highlighted.

upscattering of seed NIR/UV photons causing the prompt optical flash.

### 5.3 Dust extinction, luminosity, and energetics

Figure 11 shows the optical afterglow curve of GRB 080603A moved to a common  $z = 1$  and corrected for the large dust extinction due to the sightline within the host galaxy as described by Kann et al. (2006). The sample of other GRBs shown is taken from Kann et al. (2010). The afterglow of GRB 080603A ranks among the mid/bright GRBs. Although not a dark GRB according to the  $\beta_{\text{ox}} < 0.5$  definition, this is a fair example of an optically observed dim burst mainly because of the large amount of dust within the host galaxy: the value  $A_{V,z} = 0.8$  mag is indeed, among those measured with good accuracy, one of the largest observed so far (Kann et al. 2010). This agrees with the findings from GRB host-galaxy studies (Perley et al. 2009), samples of GRBs with multi-colour photometric datasets (Cenko et al. 2009), and some individual GRBs (Perley et al. 2011). Furthermore, the SED we built is one of the very few which clearly favours an LMC2 extinction profile, with possible evidence for the presence of the 2175 Å bump that has rarely been observed in GRB afterglows (Krühler et al. 2008; Elíasdóttir et al. 2009; Perley et al. 2011).

We could not directly measure the peak energy  $E_p$  of the prompt  $\gamma$ -ray spectrum; nevertheless, from the intermediate value of the photon index,  $\Gamma = 1.6$ , we can conservatively assume  $E_{p,i} = 160_{-130}^{+920}$  keV. Combining this with the isotropic-equivalent radiated energy,  $E_{\text{iso}} = (2.2 \pm 0.8) \times 10^{52}$  erg, GRB 080603A does not violate the  $E_{p,i} - E_{\text{iso}}$  (Amati et al. 2002; Amati 2010) relation.

Interpreting the late-time break as being due to a jet, we can provide an estimate of its opening angle, which in the ISM case turns out to be  $\theta_j = 5.7(-1.2, +1.5)$  (Sari et al.

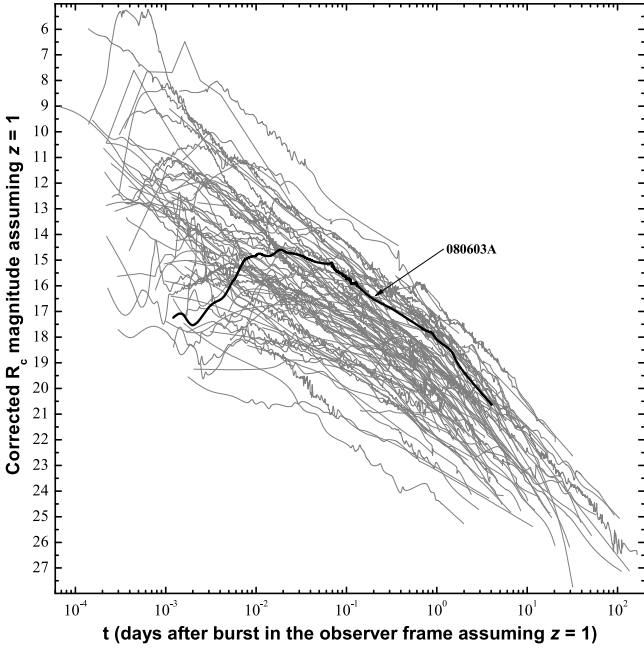


**Figure 11.** The optical afterglow light curve of GRB 080603A (thick line) moved to a common redshift of 1 and compared with the analogous sample of long GRBs (grey lines) taken from Kann et al. (2010). All afterglow curves have been corrected for dust extinction.

1999). We assumed standard values for the energy conversion efficiency,  $\eta_\gamma = 0.2$  and for the particle density of the circumburst environment,  $n = 3 \text{ cm}^{-3}$ . The collimation-corrected released energy is  $E_\gamma = (1.1 \pm 0.4) \times 10^{50}$  erg. This agrees well with the expectations of the  $E_{p,i} - E_\gamma$  relation (Ghirlanda et al. 2004, 2007), although the large uncertainty in  $E_{p,i}$  leaves this open. Calculating the analogous values in the case of a wind profile (Nava et al. 2006), these are very similar, although this density profile is disfavoured from the afterglow rise slope (Section 5.1.2):  $\theta_j = 5^\circ 1(-0^\circ 9, +1^\circ 4)$  and  $E_\gamma = (0.9 \pm 0.3) \times 10^{50}$  erg for the wind. Such an opening angle for the possible jet is very typical (Zeh et al. 2006; Nava et al. 2006; Racusin et al. 2009).

## 6 SUMMARY AND CONCLUSIONS

GRB 080603A exhibits a number of properties which allow us to strongly test many aspects of the prompt and afterglow emission standard model. Our broadband dataset spans from the prompt  $\gamma$ -rays out to the radio band 13 days post burst, and also includes spectroscopic observations of the afterglow as well as late-time photometry of the host galaxy. The main features of GRB 080603A are as follows:

- a faint ( $R \approx 20$  mag) optical flash coincident with the last episode of a two-pulse, 150-s long  $\gamma$ -ray prompt burst;
- a subsequent achromatic steep rise and peak around 1600 s, which probably marks the afterglow onset;
- no evidence for reverse-shock emission;
- ISM circumburst environment favoured from afterglow modelling;
- peak in the radio light curve detected at  $\sim 5$  days, likely caused by the passage of the synchrotron spectrum peak;

- late-time break in the afterglow light curve, interpreted as a jet break; the corresponding opening angle is  $\theta_j = 5^\circ 7(-1^\circ 2, +1^\circ 5)$ ;
- isotropic-equivalent  $\gamma$ -ray released energy  $E_{\text{iso}} = (2.2 \pm 0.8) \times 10^{52}$  erg and a collimation-corrected value of  $E_\gamma = (1.1 \pm 0.4) \times 10^{50}$  erg, both typical for long GRBs;
- remarkable dust extinction within the host galaxy,  $A_{V,z} = 0.80 \pm 0.13$  mag, that can be fit with an LMC2 profile (with marginal evidence for the 2175 Å bump), and cannot be fit by the average MW and SMC curves, at variance with most GRB extinction profiles;
- a comparable host-galaxy extinction (LMC;  $A_V = 0.77$  mag) is required for fitting the host SED, possibly suggesting that the afterglow is being extinguished by a typical sightline through the host ISM;
- extinction-corrected optical afterglow luminosity that lies in the mid-to-bright end of the distribution of GRBs at known redshift; and
- projected offset from the host galaxy centre  $< 6$  kpc, well within the offset distribution of long GRBs.

Overall, the standard afterglow model seems to account for almost all of the observed properties of the broadband afterglow evolution. In particular, the best solution is given by an electron energy index distribution of  $p = 2$ , with both cooling and injection frequencies below the optical band at the time of the peak. However, the temporal evolution of the characteristic frequencies of the synchrotron spectrum can hardly be explained assuming typical values for the micro-physical parameters.

We have constrained and crosschecked the Lorentz factor in different ways: interpreting the optical afterglow peak as the fireball deceleration yields  $\Gamma = 130 \pm 20$ . Secondly, following Zou & Piran (2010), we exploited the presence of a quiescent time between the two  $\gamma$ -ray pulses and derived an upper limit to  $\Gamma$  of 220. Finally, we focused on the optical and  $\gamma$ -ray prompt radiation to test whether inverse Compton could be a viable mechanism to explain the GRB, and found that the allowed range for  $\Gamma$  is not compatible with the estimate derived from the afterglow properties (Fig. 10; Piran et al. 2009). Alternative interpretations of the optical flash, such as a reverse-shock origin, are excluded by the gap between the flash and the afterglow onset. Instead, an interesting possibility is that of an optical flash due to internal shocks with a narrow distribution of ejecta Lorentz factors at larger radii. This would explain both the optical flash being temporally disjoint from the afterglow onset and the peaky profile of the latter (Mészáros & Rees 1999; Panaitescu & Vestrand 2011).

As an alternative to interpreting the optical afterglow peak as the fireball deceleration, the off-axis scenario requires an observer line of sight slightly off the jet cone, with  $(\theta_{\text{obs}} - \theta_j) \approx 1^\circ$ . The observed steep rise requires a structured jet with most of the energy in the jet core, with  $q \approx 4$  for an angular profile modelled as  $\mathcal{E}(\theta) \propto (\theta/\theta_j)^{-q}$  (Panaitescu & Vestrand 2008).

Summing up, the clues derived for GRB 080603A to understand the nature of the prompt emission of GRBs highlight the importance of combining broadband campaigns and deep ( $R > 20$  mag), rapid follow-up observations capable of exploring the faint end of the prompt optical emission.

## ACKNOWLEDGMENTS

C.G. acknowledges ASI for financial support (ASI-INAF contract I/088/06/0). D.A.K. acknowledges support by grant DFG K1766/16-1, U. Laux for obtaining the TLS observations, and S. Ertel for kindly granting him observing time. J.X.P. is partially supported by NASA/*Swift* grants NNG08A099G, NNX10AI18G and US National Science Foundation (NSF) CAREER grant AST-0548180. A.G. acknowledges founding from the Slovenian Research Agency and from the Centre of Excellence for Space Sciences and Technologies SPACE-SI, an operation partly financed by the European Union, the European Regional Development Fund, and the Republic of Slovenia, Ministry of Higher Education, Science, and Technology. A.V.F.'s group at U.C. Berkeley has been supported by NASA/*Swift* Guest Investigator grants NNX09AL08G, NNX10AI21G, and GO-7100028, as well as by NSF grant AST-0908886 and the TABASGO Foundation. KAIT and its ongoing operation were made possible by donations from Sun Microsystems, Inc., the Hewlett-Packard Company, AutoScope Corporation, Lick Observatory, the NSF, the University of California, the Sylvia & Jim Katzman Foundation, and the TABASGO Foundation. Some of the data presented herein were obtained at the W.M. Keck Observatory, which is operated as a scientific partnership among the California Institute of Technology, the University of California, and NASA; the observatory was made possible by the generous financial support of the W.M. Keck Foundation.

## REFERENCES

- Achterberg A., Gallant Y.A., Kirk J.G., Guthmann A.W., 2001, *MNRAS*, 328, 393
- Akerlof C., et al., 1999, *Nature*, 398, 400
- Alard C., Lupton R. H., 1998, *ApJ*, 503, 325
- Amati L., et al., 2002, *A&A*, 390, 81
- Amati L., 2010, in “The Shocking Universe — Gamma-Ray Bursts and High-Energy Shock Phenomena” (proceedings of a meeting held in Venice, September 2009) (arXiv:1002.2232)
- Band D., et al. 1993, *ApJ*, 413, 281
- Bertin E., Arnouts S., 1996, *A&AS*, 117, 393
- Beskin G., Karpov S., Bondar S., Greco G., Guarnieri A., Bartolini C., Piccioni A., 2010, *ApJ*, 719, L10
- Beuermann K., et al., 1999, *A&A*, 352, L26
- Blake C.H., et al., 2005, *Nature*, 435, 181
- Bloom J. S., Kulkarni S. R., Djorgovski S. G., 2002, *AJ*, 123, 1111
- Bloom J. S., et al., 2009, *ApJ*, 691, 723
- Boër M., Atteia J.L., Damerdjy Y., Gendre B., Klotz A., Stratta G., 2006, *ApJ*, 638, L71
- Bolzonella M., Miralles J.-M., Pelló R., 2000, *A&A*, 363, 476
- Calzetti D., Armus L., Bohlin R. C., Kinney A. L., Koornneeff J., Storchi-Bergmann T., 2000, *ApJ*, 533, 682
- Campana S., Thöne C.C., de Ugarte Postigo A., Tagliaferri G., Moretti A., Covino S., 2010, *MNRAS*, 402, 2429
- Cardelli J.A., Clayton G.C., Mathis J.S., 1989, *ApJ*, 345, 245
- Cenko S.B., et al., 2006, *ApJ*, 652, 490
- Cenko S.B., et al. 2009, *ApJ*, 693, 1484
- Chandra P., Frail D., 2008a, *GCN Circ.*, 7843
- Chandra P., Frail D., 2008b, *GCN Circ.*, 7855
- Chen H.-W., et al., 2009, *ApJ*, 691, 152
- Chornock R., Perley D., Li W., Filippenko A.V., 2008, *GCN Circ.*, 7789
- Covino S., et al., 2010, *A&A*, 521, A53
- Curran P. A., Evans P. A., de Pasquale M., Page M. J., van der Horst A. J., 2010, *ApJ*, 716, L135
- Daigne F., Bosnjak Z., Dubus G., 2011, *A&A*, 526, A110
- Eichler D., Granot J. 2006, *ApJ*, 641, L5
- Elíasdóttir Á, et al., 2009, *ApJ*, 697, 1725
- Evans P.A., et al., 2009, *MNRAS*, 397, 1177
- Fitzpatrick E.L., Massa D., 1990, *ApJS*, 72, 163 (FM)
- Fukugita M., Shimasaku K., Ichikawa T., 1995, *PASP*, 107, 945
- Fukugita M., et al., 1996, *AJ*, 111, 1748
- Gehrels N., et al., 2004, *ApJ*, 611, 1005
- Ghirlanda G., Ghisellini G., Lazzati D., 2004, *ApJ*, 616, 331
- Ghirlanda G., Nava L., Ghisellini G., Firmani C., 2007, *A&A*, 466, 127
- Ghisellini G., Celotti A., Lazzati D., 2000, *MNRAS*, 313, L1
- Gomboc A., et al., 2008, *GCN Circ.*, 7788
- Gordon K.D., Clayton G.C., Misselt K.A., Landolt A.U., Wolff M.J., 2003, *ApJ*, 594, 279
- Granot J., Panaitescu A., Kumar P., Woosley S.E., 2002, *ApJ*, 570, L61
- Granot J., Nakar E., Piran T., 2003, *Nature*, 426, 138
- Granot J., Ramirez-Ruiz E., Perna R. 2005, *ApJ*, 630, 1003
- Greiner J., et al. 2009, *ApJ*, 693, 1912
- Guidorzi C., et al., 2006, *PASP*, 118, 288
- Guidorzi C., et al., 2009, *A&A*, 499, 439
- Guidorzi C., Lacapra M., Frontera F., Montanari E., Amati L., Calura F., Nicastro L., Orlandini M., 2011, *A&A*, 526, A49
- Guiries S., et al., 2010, *ApJ*, 725, 225
- Jin Z.P., Fan Y.Z., 2007, *MNRAS*, 378, 1043
- Jordi K., Grebel E.K., Ammon K., 2006, *A&A*, 460, 339
- Kalberla P.M.W. et al., 2005, *A&A*, 440, 775
- Kaneko Y., Preece R.D., Briggs M.S., Paciesas W.S., Meegan C.A., Band D.L., 2006, *ApJS*, 166, 298
- Kann D.A., Klose S., Zeh A., 2006, *ApJ*, 641, 993
- Kann D.A., Laux U., Ertel S., 2008, *GCN Circ.*, 7822
- Kann D.A., et al. 2010, *ApJ*, 720, 1513
- Kann D.A., et al. 2011, *ApJ*, 734, 96
- Kistler M.D., Yüksel H., Beacom J.F., Hopkins A.M., Wyithe J.S.B., 2009, *ApJ*, 705, L104
- Klotz A., Gendre B., Stratta G., Atteia J.L., Boër M., Malacrino F., Damerdjy Y., Behrend R., 2006, *A&A*, 451, L39
- Klotz A., Gendre B., Atteia J.L., Boër M., Coward D.M., Imerito C., 2009, *A&A*, 697, L18
- Klunko E., Pozanenko A., 2008, *GCN Circ.*, 7887
- Kobayashi S., 2000, *ApJ*, 545, 807
- Kobayashi S., Sari R., 2000, *ApJ*, 542, 819
- Kobayashi S., Zhang B., 2003a, *ApJ*, 582, L75
- Kobayashi S., Zhang B., 2003b, *ApJ*, 597, 455
- Kobayashi S., Zhang B., 2007, *ApJ*, 655, 973
- Krühler T., et al. 2008, *ApJ*, 685, 376
- Krühler T., et al. 2009, *A&A*, 508, 593

- Kuin N.P.M., Mangano V., 2008, *GCN Circ.*, 7804
- Kumar P., Granot J. 2003, *ApJ*, 591, 1075
- Kumar P., McMahon E., 2008, *MNRAS*, 384, 33
- Landolt A.U., 1992, *AJ*, 104, 340
- Lebrun F., et al., 2003, *A&A*, 411, L141
- Levesque E.M., Soderberg A.M., Kewley L.J., Berger E., 2010, *ApJ*, 725, 1337
- Li W., Filippenko A.V., Chornock R., & Jha S., 2003, *PASP*, 115, 844
- Liang E.W., Yi S.X., Lü H.J., Zhang B.B., Zhang B., 2010, *ApJ*, 725, 2209
- Lloyd N.M., Petrosian V., 2000, *ApJ*, 543, 722
- Margutti R., et al., 2010, *MNRAS*, 402, 46
- Melandri A., et al., 2008, *ApJ*, 686, 1209
- Melandri A., et al., 2009, *MNRAS*, 395, 1941
- Melandri A., et al. 2010, *ApJ*, 723, 1331
- Mereghetti S., Götz D., Borkowski J., Walter R., Pedersen H., 2003, *A&A*, 411, L291
- Mészáros P., Rees M.J., 1997, *ApJ*, 476, 232
- Mészáros P., Rees M.J., 1999, *MNRAS*, 306, L39
- Mészáros P., 2006, *Rep. Prog. Phys.*, 69, 2259
- Miller A.A., Bloom J.S., Perley D.A., 2008, *GCN Circ.*, 7826
- Milne P.A., Updike A., 2008, *GCN Circ.*, 7793
- Molinari E., et al., 2007, *A&A*, 469, L13
- Morrison R., McCammon D., 1983, *ApJ*, 270, 119
- Mundell C.G., et al., 2007, *ApJ*, 660, 489
- Nava L., Ghisellini G., Ghirlanda G., Tavecchio F., Firmani C., 2006, *A&A*, 450, 471
- Norris J.P., Nemiroff R.J., Bonnell J.T., Scargle J.D., Kouveliotou C., Paciesas W.S., Meegan C.A., Fishman G.J., 1996, *ApJ*, 459, 393
- Norris J.P., Bonnell J.T., Kazanas D., Scargle J.D., Hakkila J., Giblin T.W., 2005, *ApJ*, 627, 324
- Nysewander M., Reichart D.E., Crain J.A., Foster A., Haislip J., Ivarsen K., Lacluyze A., Trotter A., 2009, *ApJ*, 693, 1417
- Nysewander M., Fruchter A.S., Pe'er A., 2009b, *ApJ*, 701, 824
- Oates S. R., et al., 2009, *MNRAS*, 395, 490
- Oke J. B., et al., 1995, *PASP*, 107, 375
- Page K.L., et al., 2009, *MNRAS*, 400, 134
- Paizis A., Mereghetti S., Gotz D., Turler M., Beckmann V., Beck M., Borkowski J., 2008, *GCN Circ.*, 7790
- Panaitescu A., Mészáros P., Rees M.J., 1998, *ApJ*, 503, 314
- Panaitescu A., Kumar P., 2002, *ApJ*, 571, 779
- Panaitescu A., 2005, *MNRAS*, 362, 921
- Panaitescu A., Vestrand W.T., 2008, *MNRAS*, 387, 497
- Panaitescu A., Vestrand W.T., 2011, *MNRAS*, 414, 3537
- Pei Y.C., 1992, *ApJ*, 395, 130
- Perley D.A., Bloom J.S., Prochaska J.X., 2008a, *GCN Circ.*, 7791
- Perley D.A., Bloom J.S., Miller A.A., Shiode J., Brewer J., Starr D., Kennedy R., 2008b, *GCN Circ.*, 7870
- Perley D.A., et al. 2008c, *ApJ*, 672, 449
- Perley D.A., et al. 2009, *AJ*, 138, 1690
- Perley D.A., et al. 2010, *MNRAS*, 406, 2473
- Perley D.A., et al. 2011, *AJ*, 141, 36
- Piran T., Sari R., Zou Y.-C., 2009, *MNRAS*, 393, 1107
- Preece R.D., Briggs M.S., Malozzi R.S., Pendleton G.N., Paciesas W.S., Band D.L. 1998, *ApJ*, 506, L23
- Prochaska J.X., Chen H.-W., Bloom J.S. 2006, *ApJ*, 648, 95
- Prochaska J.X., Chen H.-W., Dessauges-Zavadsky M., Bloom J.S. 2007, *ApJ*, 666, 267
- Prochaska J.X., et al., 2009, *ApJ*, 691, L27
- Prochter G.E., Prochaska J.X., Chen H.-W. 2006, *ApJ*, 648, L93
- Racusin J.L., et al., 2008, *Nature*, 455, 183
- Racusin J.L., et al., 2009, *ApJ*, 698, 43
- Rees M.J., Mészáros P., 1992, *MNRAS*, 258, 42
- Rees M.J., Mészáros P., 1998, *ApJ*, 496, L1
- Robertson B.E., Ellis R.S., Dunlop J.S., McLure R.J., Stark D.P., 2010, *Nature*, 468, 49
- Roming P.W.A., et al., 2009, *ApJ*, 690, 163
- Rossi A., et al., 2011, *A&A*, 529, A142
- Rumyantsev V., Pozanenko A., 2008a, *GCN Circ.*, 7860
- Rumyantsev V., Pozanenko A., 2008b, *GCN Circ.*, 7883
- Rumyantsev V., Antoniuk K., Klunko E., Pozanenko A., 2008, *GCN Circ.*, 7976
- Rykoff E.S., et al., 2004, *ApJ*, 601, 1013
- Rykoff E.S., et al., 2005, *ApJ*, 631, L121
- Rykoff E.S., et al., 2009, *ApJ*, 702, 489
- Sakamoto T., et al., 2008, *ApJ*, 679, 570
- Sakamoto T., et al., 2009, *ApJ*, 693, 922
- Salvaterra R., et al., 2009, *Nature*, 461, 1258
- Sari R., 1997, *ApJ*, 489, L37
- Sari R., Piran T., Narayan R., 1998, *ApJ*, 497, L17
- Sari R., Piran T., 1999, *ApJ*, 520, 641
- Sari R., Piran T., Halpern J.P., 1999, *ApJ*, 519, L17
- Sari R., Mészáros, P., 2000, *ApJ*, 535, L33
- Savaglio S., Glazebrook K., Le Borgne D., 2009, *ApJ*, 691, 182
- Sbarufatti B., Mangano V., La Parola V., 2008a, *GCN Circ.*, 7810
- Sbarufatti B., Kuin P., Barthelmy S.D., Burrows D.N., Roming P., Gehrels N., 2008b, *GCN Rep.*, 146.1
- Schlegel D.J., Finkbeiner D.P., Davis M., 1998, *ApJ*, 500, 525
- Smith J.A., et al., 2002, *AJ*, 123, 2121
- Spergel D.N., et al., 2003, *ApJS*, 148, 175
- Spitkovsky A., 2008, *ApJ*, 682, L5
- Starling R.L.C., van der Horst A.J., Rol E., Wijers R.A.M.J., Kouveliotou C., Wieserma K., Curran P.A., Weltevrede P., 2008, *ApJ*, 672, 433
- Stratta G., et al., 2009, *A&A*, 503, 783
- Tanvir N.R., et al., 2009, *Nature*, 461, 1254
- Thöne C.C., et al., 2010, *A&A*, 523, A70
- Vestrand W.T., et al., 2005, *Nature*, 435, 178
- Vestrand W.T., et al., 2006, *Nature*, 442, 172
- Vianello G., Götz D., Mereghetti S., 2009, *A&A*, 495, 1005
- Wei D.M., 2007, *MNRAS*, 374, 525
- Winkler C., et al., 2003, *A&A*, 411, L1
- Yamazaki R., Ioka K., Nakamura T. 2002, *ApJ*, 571, L31
- Yost S.A., et al., 2007, *ApJ*, 657, 925
- Yuan F., et al. 2010, *ApJ*, 711, 870
- Zeh A., Klose S., Kann D.A., 2006, *ApJ*, 637, 889
- Zhang B., Mészáros P., 2002, *ApJ*, 571, 876
- Zhang B., Kobayashi S., Mészáros P., 2003, *ApJ*, 595, 950
- Zhang B., Fan Y.Z., Dyks J., Kobayashi S., Mészáros P., Burrows D.N., Nousek J.A., Gehrels N., 2006, *ApJ*, 642, 354
- Zou Y.-C., Piran T. 2010, *MNRAS*, 402, 1854

**Table 8.** Photometric data set of the NIR/optical afterglow of GRB 080603A. Uncertainties are  $1\sigma$ .

Time <sup>a</sup> (s)	Telescope	Exp. (s)	Filter	Magnitude <sup>b</sup>	Flux <sup>c</sup> ( $\mu$ Jy)	Time <sup>a</sup> (s)	Telescope	Exp. (s)	Filter	Magnitude <sup>b</sup>	Flux <sup>c</sup> ( $\mu$ Jy)
105	FTN	10	<i>R</i>	20.78 ± 0.26	16.7 ± 4.5	94762	FTN	600	<i>i'</i>	21.33 ± 0.12	11.6 ± 1.4
136	FTN	10	<i>R</i>	20.45 ± 0.25	22.7 ± 5.9	286	KAIT	15	<i>I</i>	> 17.00	< 627
167	FTN	10	<i>R</i>	21.40 ± 0.52	9.4 ± 5.8	414	KAIT	45	<i>I</i>	> 17.30	< 476
558	FTN	30	<i>R</i>	18.93 ± 0.05	91.8 ± 4.3	604	KAIT	60	<i>I</i>	17.90 ± 0.50	274 ± 160
883	FTN	60	<i>R</i>	18.31 ± 0.03	162.6 ± 4.6	860	KAIT	180	<i>I</i>	17.60 ± 0.17	361 ± 61
1381	FTN	120	<i>R</i>	18.30 ± 0.03	164.1 ± 4.6	1165	KAIT	60	<i>I</i>	> 17.50	< 396
2112	FTN	180	<i>R</i>	18.27 ± 0.03	168.7 ± 4.7	252	FTN	10	<i>B</i>	21.73 ± 0.36	10.3 ± 4.1
2927	FTN	120	<i>R</i>	18.40 ± 0.03	149.6 ± 4.2	478	FTN	30	<i>B</i>	20.66 ± 0.10	27.6 ± 2.7
3745	FTN	180	<i>R</i>	18.61 ± 0.03	123.3 ± 3.5	772	FTN	60	<i>B</i>	19.73 ± 0.04	65.0 ± 2.4
5846	FTN	72	<i>R</i>	18.72 ± 0.05	111.4 ± 5.3	1209	FTN	120	<i>B</i>	19.76 ± 0.03	63.2 ± 1.8
6280	FTN	30	<i>R</i>	18.86 ± 0.05	98.0 ± 4.6	1881	FTN	180	<i>B</i>	19.62 ± 0.03	71.9 ± 2.0
6621	FTN	60	<i>R</i>	18.95 ± 0.04	90.2 ± 3.4	2757	FTN	120	<i>B</i>	19.72 ± 0.04	65.6 ± 2.5
7110	FTN	120	<i>R</i>	19.04 ± 0.04	83.0 ± 3.1	3511	FTN	180	<i>B</i>	19.88 ± 0.03	56.6 ± 1.6
7832	FTN	180	<i>R</i>	19.10 ± 0.03	78.5 ± 2.2	5968	FTN	10	<i>B</i>	19.94 ± 0.18	53.6 ± 9.7
8569	FTN	120	<i>R</i>	19.26 ± 0.04	67.8 ± 2.5	6195	FTN	30	<i>B</i>	20.07 ± 0.08	47.5 ± 3.6
9258	FTN	180	<i>R</i>	19.30 ± 0.03	65.3 ± 1.8	6510	FTN	60	<i>B</i>	20.24 ± 0.07	40.6 ± 2.7
9552	FTN	30	<i>R</i>	19.25 ± 0.07	68.4 ± 4.6	6935	FTN	120	<i>B</i>	20.28 ± 0.05	39.2 ± 1.8
9903	FTN	60	<i>R</i>	19.43 ± 0.06	58.0 ± 3.3	7596	FTN	180	<i>B</i>	20.40 ± 0.04	35.1 ± 1.3
10414	FTN	120	<i>R</i>	19.43 ± 0.04	58.0 ± 2.2	8401	FTN	120	<i>B</i>	20.48 ± 0.05	32.6 ± 1.5
11164	FTN	180	<i>R</i>	19.50 ± 0.04	54.3 ± 2.0	9027	FTN	180	<i>B</i>	20.55 ± 0.05	30.5 ± 1.4
25879	AZT33	960	<i>R</i>	20.37 ± 0.08	24.4 ± 1.9	9468	FTN	30	<i>B</i>	20.70 ± 0.12	26.6 ± 3.1
31242	AZT11	1800	<i>R</i>	20.56 ± 0.13	20.5 ± 2.6	9783	FTN	60	<i>B</i>	20.82 ± 0.09	23.8 ± 2.1
56857	LT	1860	<i>r'</i>	21.60 ± 0.08	9.3 ± 0.7	10244	FTN	120	<i>B</i>	20.82 ± 0.07	23.8 ± 1.6
134128	TLS	1800	<i>R</i>	22.1 ± 0.3	5.0 ± 1.6	10924	FTN	180	<i>B</i>	20.77 ± 0.05	24.9 ± 1.2
134490	Z1000	1620	<i>R</i>	22.52 ± 0.25	3.4 ± 0.9	350436	Keck	785	<i>g'</i>	24.95 ± 0.20	0.449 ± 0.091
306753	Z1000	4290	<i>R</i>	> 22.9	< 2.4	310	FTN	10	<i>V</i>	20.76 ± 0.25	20.6 ± 5.3
350436	Keck	690	<i>R</i>	24.17 ± 0.14	0.74 ± 0.10	6025	FTN	10	<i>V</i>	19.38 ± 0.10	73.4 ± 7.1
382	FTN	10	<i>i'</i>	19.62 ± 0.16	56.1 ± 8.9	260	KAIT	15	<i>V</i>	> 17.20	< 547
651	FTN	30	<i>i'</i>	18.05 ± 0.03	238.4 ± 6.7	358	KAIT	45	<i>V</i>	> 17.70	< 345
1017	FTN	60	<i>i'</i>	17.90 ± 0.03	273.7 ± 7.7	532	KAIT	60	<i>V</i>	18.60 ± 0.70	151 ± 136
1598	FTN	120	<i>i'</i>	17.62 ± 0.03	354.2 ± 9.9	315	KAIT	20	clear	> 18.00	< 216
2433	FTN	180	<i>i'</i>	17.87 ± 0.03	281.3 ± 7.9	468	KAIT	45	clear	18.63 ± 0.47	121 ± 66
3156	FTN	120	<i>i'</i>	18.04 ± 0.03	240.6 ± 6.7	674	KAIT	60	clear	18.40 ± 0.29	150 ± 46
6100	FTN	10	<i>i'</i>	18.41 ± 0.07	171.1 ± 11.4	958	KAIT	180	clear	18.17 ± 0.12	185 ± 22
6375	FTN	30	<i>i'</i>	18.47 ± 0.04	161.9 ± 6.1	70327	PAIRITEL	2282	<i>J</i>	18.70 ± 0.19	54.7 ± 10.5
6755	FTN	60	<i>i'</i>	18.59 ± 0.04	145.0 ± 5.4	81686	PAIRITEL	4363	<i>J</i>	18.92 ± 0.21	44.7 ± 9.5
7325	FTN	120	<i>i'</i>	18.61 ± 0.04	142.3 ± 5.3	70327	PAIRITEL	2282	<i>H</i>	17.82 ± 0.16	78.0 ± 12.4
8107	FTN	180	<i>i'</i>	18.74 ± 0.03	126.2 ± 3.5	81686	PAIRITEL	4363	<i>H</i>	17.81 ± 0.15	78.8 ± 11.7
8770	FTN	120	<i>i'</i>	18.87 ± 0.03	112.0 ± 3.1	70327	PAIRITEL	2282	<i>K</i>	17.14 ± 0.18	94.3 ± 17.0
9650	FTN	30	<i>i'</i>	18.99 ± 0.06	100.3 ± 5.7	81686	PAIRITEL	4363	<i>K</i>	16.82 ± 0.16	127 ± 20
10035	FTN	60	<i>i'</i>	19.02 ± 0.04	97.5 ± 3.7	6444	GeminiN	60	<i>r'</i>	19.10 ± 0.03	93 ± 3
10628	FTN	120	<i>i'</i>	19.06 ± 0.03	94.0 ± 2.6						
11462	FTN	180	<i>i'</i>	19.10 ± 0.03	90.6 ± 2.5						
60662	LT	1860	<i>i'</i>	20.79 ± 0.06	19.1 ± 1.1						
77486	FTN	1591	<i>i'</i>	20.92 ± 0.06	17.0 ± 1.0						

<sup>a</sup>Midpoint time from the GRB onset time.

<sup>b</sup>Corrected for airmass.

<sup>c</sup>Corrected for Galactic extinction.

**Table 9.** Equivalent-width measurements for GRB 080603A

$\lambda_{\text{obs}}$ [Å]	$\lambda_{\text{rest}}$ [Å]	$z$	Feature	$\text{EW}_{\text{obs}}$ [Å]	$\lambda_{\text{obs}}$ [Å]	$\lambda_{\text{rest}}$ [Å]	$z$	Feature	$\text{EW}_{\text{obs}}$ [Å]
4986.81	1854.72	1.6874	Al III	$5.10 \pm 0.42$	7025.48	2612.65	1.6874	FeII*	$1.80 \pm 0.06$
5008.66	1862.79	1.6874	Al III	$4.26 \pm 0.39$		2614.61	1.6874	FeII*	
5325.57	2344.21	1.2714	Fe II	$3.72 \pm 0.15$	7039.98	2618.40	1.6874	FeII*	$0.55 \pm 0.06$
5393.70	2374.46	1.2714	Fe II	$2.52 \pm 0.17$		2621.19	1.6874	FeII*	
5413.14	2382.76	1.2714	Fe II	$4.46 \pm 0.15$	7051.45	2622.45	1.6874	FeII*	$0.17 \pm 0.05$
	2012.17	1.6874	Co II		7062.18	2626.45	1.6874	FeII*	$0.88 \pm 0.06$
5447.13	2026.14	1.6874	Zn II	$2.92 \pm 0.15$		2629.08	1.6874	FeII*	
	2026.27	1.6874	Cr II		7075.84	2631.83	1.6874	FeII*	$1.23 \pm 0.05$
	2026.48	1.6874	Mg I			2632.11	1.6874	FeII*	
5528.99	2056.25	1.6874	Cr II	$1.36 \pm 0.14$	7169.21	2796.35	1.5636	MgII	$1.98 \pm 0.05$
5545.03	2062.23	1.6874	Cr II	$2.12 \pm 0.14$	7187.26	2803.53	1.5636	MgII	$2.82 \pm 0.07$
	2062.66	1.6874	Zn II		7201.86	2683.89	1.6874	VII	$1.38 \pm 0.08$
5852.00	2175.35	1.6874	Ni II*	$0.33 \pm 0.09$	7366.69	3242.93	1.2714	TiII	$0.59 \pm 0.06$
5875.34	2586.65	1.2714	Fe II	$3.67 \pm 0.11$		2740.36	1.6874	FeII*	
5892.87				$0.88 \pm 0.14$	7391.43	2747.31	1.6874	FeII*	$0.65 \pm 0.07$
5906.19	2600.17	1.2714	Fe II	$4.77 \pm 0.11$		2747.85	1.6874	FeII*	
6047.64	2249.88	1.6874	Fe II	$1.46 \pm 0.11$		2750.16	1.6874	FeII*	
6077.64	2260.78	1.6874	Fe II	$1.33 \pm 0.10$	7411.15	2756.56	1.6874	FeII*	$0.45 \pm 0.06$
6110.07	2382.76	1.5636	Fe II	$0.51 \pm 0.12$	7522.96	2796.35	1.6874	MgII	$35.39 \pm 0.07$
6274.04	2328.11	1.6874	Fe II*	$2.22 \pm 0.12$		2803.53	1.6874	MgII	
	2333.52	1.6874	Fe II*						
	2338.72	1.6874	Fe II*						
6296.24				$3.56 \pm 0.07$					
6301.42	2344.21	1.6874	Fe II	$6.78 \pm 0.09$					
	2345.00	1.6874	Fe II*						
6315.59	2349.02	1.6874	Fe II*	$1.00 \pm 0.08$					
6351.50	2796.35	1.2714	Mg II	$7.09 \pm 0.08$					
	2359.83	1.6874	Fe II*						
	2365.55	1.6874	Fe II*						
6368.10	2803.53	1.2714	Mg II	$7.04 \pm 0.07$					
6382.84	2374.46	1.6874	Fe II	$5.49 \pm 0.06$					
6402.91	2381.49	1.6874	Fe II*	$10.71 \pm 0.08$					
	2382.76	1.6874	Fe II						
	2383.79	1.6874	Fe II*						
6423.98	2389.36	1.6874	Fe II*	$0.77 \pm 0.07$					
6443.15	2396.15	1.6874	Fe II*	$1.39 \pm 0.07$					
	2396.36	1.6874	Fe II*						
6452.81	2399.97	1.6874	Fe II*	$0.63 \pm 0.07$					
6482.13	2852.96	1.2714	Mg I	$4.82 \pm 0.12$					
	2405.16	1.6874	Fe II*						
	2405.62	1.6874	Fe II*						
	2407.39	1.6874	Fe II*						
	2411.25	1.6874	Fe II*						
	2411.80	1.6874	Fe II*						
	2414.05	1.6874	Fe II*						
6631.47	2586.65	1.5636	Fe II	$0.21 \pm 0.06$					
6666.09	2600.17	1.5636	Fe II	$0.55 \pm 0.06$					
6886.25				$6.66 \pm 0.12$					
6926.67	2576.88	1.6874	Mn II	$2.84 \pm 0.07$					
6945.33				$2.11 \pm 0.05$					
6953.07	2586.65	1.6874	Fe II	$6.98 \pm 0.05$					
6981.10	3073.88	1.2714	Ti II	$5.99 \pm 0.06$					
	2594.50	1.6874	Mn II						
6988.76	2599.15	1.6874	Fe II*	$8.97 \pm 0.05$					
	2600.17	1.6874	Fe II						
7007.74	2606.46	1.6874	Mn II	$2.65 \pm 0.05$					
	2607.87	1.6874	Fe II*						